Clemson University
TigerPrints

All Theses | Theses

8-2012

Component Mode Synthesis Approach for Quantum Mechanical Electrostatic and Transport Analysis of Nanoscale Structures and Devices

Zhe Gao
Clemson University, zhegao22@gmail.com

Follow this and additional works at: https://tigerprints.clemson.edu/all_theses

Part of the Nanoscience and Nanotechnology Commons

Recommended Citation
Gao, Zhe, "Component Mode Synthesis Approach for Quantum Mechanical Electrostatic and Transport Analysis of Nanoscale Structures and Devices" (2012). *All Theses*. 1417.
https://tigerprints.clemson.edu/all_theses/1417

This Thesis is brought to you for free and open access by the Theses at TigerPrints. It has been accepted for inclusion in All Theses by an authorized administrator of TigerPrints. For more information, please contact kokeefe@clemson.edu.

COMPONENT MODE SYNTHESIS APPROACH FOR QUANTUM MECHANICAL ELECTROSTATIC AND TRANSPORT ANALYSIS OF NANOSCALE STRUCTURES AND DEVICES

A Thesis
Presented to
the Graduate School of
Clemson University

In Partial Fulfillment
of the Requirements for the Degree
Masters of Science
Mechanical Engineering

---

by
Zhe Gao
August 2012

Accepted by:
Dr. Gang Li, Committee Chair
Dr. Xiangchun Xuan
Dr. Huijuan Zhao

Abstract

As the dimensions of commonly used semiconductor devices have shrunk into nanometer regime, it is recognized that the influence of quantum effects on their electrostatic and transport properties cannot be ignored. In the past few decades, various computational models and approaches have been developed to analyze these properties in nanostructures and devices. Among these computational models, the Schrödinger-Poisson model has been widely adopted for quantum mechanical electrostatic and transport analysis of nanostructures and devices such as quantum wires, metal–oxide–semiconductor field effect transistors (MOSFETs) and nanoelectromechanical systems (NEMS). The numerical results allow for evaluations of the electrical properties such as charge concentration and potential profile in these structures. The emergence of MOSFETs with multiple gates, such as Trigates, FinFETs and Pi-gates, offers a superior electrostatic control of devices by the gates, which can be therefore used to reduce the short channel effects within those devices. Full 2-D electrostatic and transport analysis enables a better understanding of the scalability of devices, geometric effects on the potential and charge distribution, and transport characteristics of the transistors. The Schrödinger-Poisson model is attractive due to its simplicity and straightforward implementation by using standard numerical methods. However, as it is required to solve a generalized eigenvalue problem generated from the discretization of the Schrödinger equation, the computational cost of the analysis increases quickly when the system's degrees of freedom (DOFs) increase. For this reason, techniques that enable an efficient solution of discretized Schrödinger equation in multidimensional domains are desirable.

In this work, we seek to accelerate the numerical solution of the Schrödinger equation by using a component mode synthesis (CMS) approach. In the CMS approach, a nanostructure

is divided into a set of substructures or components and the eigenvalues (energy levels) and eigenvectors (wave functions) are computed first for all the substructures. The computed wave functions are then combined with constraint or attachment modes to construct a transformation matrix. By using the transformation matrix, a reduced-order system of the Schrödinger equation is obtained for the entire nanostructure. The global energy levels and wave functions can be obtained with the reduced-order system. Through an iteration procedure between the Schrödinger and Poisson equations, a self-consistent solution for charge concentration and potential profile can be obtained. In this work, the CMS approach is applied to compute the electrostatic and transport properties of a set of semiconductor devices including a quantum wire and several multiple-gate MOSFETs. It is demonstrated that the CMS approach greatly reduces the computational cost while giving accurate results.

Acknowledgements

I would like to thank my advisor Professor Li for his guidance on my Master's research. Without said guidance, this thesis would not have been possible. Before I came to Clemson University, I had no knowledge of the Finite Element Method. Under his tutelage, I have acquired some very advanced numerical modeling techniques in my research that will serve me well in the future.

I would also like to thank an undergraduate instructor for sparking my interest in semiconductor device modeling, Professor Hsieh. I remember it was in his class ECE 440 that I developed an appreciation for solid state electronics. His class was both engaging and different, which motivated me to do well in his class. Without this class, I would have never obtained the technical foundations necessary for the research outlined in this thesis.

Furthermore, I would like to thank Professor Xuan and Professor Zhao for taking the time out of their busy schedules to serve as committee members for my thesis defense. I would also like to thank the ME staff, particularly Tameka, for guiding me through the graduation process.

Lastly, I would like to thank my parents for their support and encouragement. Thank you for always believing in me.

Table of Contents

Abstract ii

Acknowledgements iv

List of Tables vi

List of Figures vii

1. Chapter 1 Introduction 1

1.1 Nanoscale Structures, Devices and Materials 1

1.2 Quantum Mechanical Electrostatic and Transport Models 5

1.2.1 Schrödinger-Poisson Model for Electrostatic Analysis 6

1.3.2 Schrödinger Poisson Model for Electron Transport Analysis 7

1.3.3 Nonequilibrium Green's Function Method for Electron Transport Analysis 8

1.3.4 Atomistic Models 9

1.4 Motivation of CMS based Approaches 11

2. Chapter 2 Component Mode Synthesis (CMS) Approach for Solving the Schrödinger Equation 14

2.1 Effective Mass Schrödinger Equation and Its Finite Element Formulation 14

2.2 CMS Method 18

2.3 Numerical Results 24

3. Chapter 3 Quantum Mechanical Electrostatic Analysis of Nanostructures and Nanodevices 32

3.1 Schrödinger-Poisson Approach and Finite Element Formulation 32

3.2 Numerical Results 37

4. Chapter 4 Quantum Mechanical Electrical Transport Analysis of Nanodevices 49

4.1 Quantum Transmitting Boundary Method (QTBM) 50

4.1 Numerical Results 62

5. Chapter 5 Conclusions and Future Work 69

6. References 71

List of Tables

Table 2-1: Comparison of eigenenergies obtained from the CMS and direct approaches 25

List of Figures

Figure 1-1: CMOS made from an n-type and a p-type MOSFET 2

Figure 1-2: Nanoelectromechanical Systems (NEMS). Left: a nanoswitch [4]. Right: an ultra-high frequency nanoresonator [5]. 3

Figure 1-3: Nanostructured materials. Left: nanostructured microsensor [18]. Nanocomposite thermoelectric material [20]. 4

Figure 2-1: An example of isoparametric mapping of 4-node linear quadrilateral elements. 16

Figure 2-2: Schematic of the component mode synthesis approach for solving the Schrödinger equation. 19

Figure 2-3: Computational domain of a double gate MOSFET. 24

Figure 2-4: "Cosine" mode wave function solutions for the MOSET. Left column: direct solutions of the full eigensystem. Right column: CMS solutions. Top to bottom: 1st to 5th wave functions. 40 by 10 mesh domain. 27

Figure 2-5: computational domain of a quantum wire 29

Figure 2-6: Wave function solutions for the quantum wire. Left column: direct solutions of the full eigensystem. Right column: CMS solutions. Top to bottom: 1st to 5th wave functions. 40 by 40 mesh domain. 31

Figure 3-1: Computational domain of a quantum wire. 38

Figure 3-2: Electron density solutions obtained from the direct method for (a) -0.3V and (b) 0.3V applied to the outer boundary, and density solutions from the CMS approach for (c) -0.3V and (d) 0.3V applied to outer boundary. 60 by 60 mesh domain. 39

Figure 3-3: Potential energy solutions ($e\phi$) obtained from the direct method for (a) -0.3V and (b) 0.3V applied to the outer boundary, and potential energy solutions from the CMS approach for (c) -0.3V and (d) 0.3V applied to outer boundary. 60 by 60 mesh domain. 40

Figure 3-4: A comparison of the CPU time for meshes of different sizes. 40

Figure 3-5: Relative error of the eigenvalues obtained from the CMS approach compared with the results obtained from the direct method on a 80 by 80 mesh with Dirichlet boundary conditions. 41

Figure 3-6: Density solutions for the Neumann boundary case: (a) direct approach and (b) CMS approach. 60 by 60 mesh domain. 43

Figure 3-7: Potential energy solutions for the Neumann boundary case (a) direct approach (b) CMS approach. 60 by 60 mesh domain. 43

Figure 3-8: Relative error of the eigenvalues obtained from the CMS approach compared with the results obtained from the direct method on a 80 by 80 mesh with Neumann boundary conditions. 44

Figure 3-9: Computational domain of an all-around MOSFET. 46

Figure 3-10: Electron density solutions for the all-around MOSFET: (a) direct approach (b) CMS approach. 60 by 60 mesh domain. 46

Figure 3-11: Potential energy solutions for the all-around MOSFET: (a) direct approach (b) CMS approach. 60 by 60 mesh domain. 47

Figure 3-12: Comparison of the CPU times for a single ladder for meshes of different sizes. 47

Figure 3-13: Relative error of eigenvalues of the 3 ladders for an 80 by 80 mesh. Legend indicates the relative effective masses in (x,y,z) directions for silicon. 48

Figure 4-1: 2-D simulation domain for electron transport analysis. 51

Figure 4-2: Double-gate MOSFET and its simulation domains. 63

Figure 4-3: Numerical solutions obtained from QTBM for Vg=0V. Left: potential energy. Right: electron density. 40 by 10 mesh domain. 64

Figure 4-4: Numerical solutions obtained from CMS based QTBM for Vg=0V. Left: potential energy. Right: electron density. 40 by 10 mesh domain. 65

Figure 4-5: Numerical solutions obtained from QTBM for Vg=0.2V. Left: potential energy. Right: electron density. 40 by 10 mesh domain. 65

Figure 4-6: Numerical solutions obtained from CMS based QTBM for Vg=0.2V. Left: potential energy. Right: electron density. 40 by 10 mesh domain. 66

Figure 4-7: Numerical solutions obtained from QTBM for Vg=0.4V. Left: potential energy. Right: electron density. 40 by 10 mesh domain. 66

Figure 4-8: Numerical solutions obtained from CMS based QTBM for Vg=0.4V. Left: potential energy. Right: electron density. 40 by 10 mesh domain. 67

Figure 4-9: Comparison of the CPU times for meshes of different sizes: 10 retained eigenvalues. 67

Figure 4-10: Comparison of the CPU times for meshes of different sizes: 40 retained eigenvalues. 68

Chapter 1 Introduction

1.1 Nanoscale Structures, Devices and Materials

Over the past 30 years, the die size of Intel transistors has decreased from 3 micrometers (Intel 8086) down to currently 32 (Sandy Bridge) and 22 nanometers (Ivy Bridge) [1]. This reduction in size has allowed the number of transistors to increase from 29,000 in 1978 to over a billion currently. This drastic increase in the number of transistors is correlated with a drastic increase in computing power. Currently, complimentary metal-on-oxide semiconductor (CMOS) technology is preferred due to the low power consumption property in which the CMOS only consumes power when the inputs are being switched [2]. In general, a transistor can be thought of as a switch. A CMOS can be made from 2 complimentary metal-oxide-semiconductor field effect transistors (MOSFETs), as shown in Figure 1-1. For n-MOS transistors, an input signal ("V_{in}" in Figure 1-1) of a "1" (high voltage) indicates the "on" state whereas for the p-MOS, an input signal of a "0" (low voltage) indicates the "on" state. When the n-MOS is on, the p-MOS is off, limiting the current from V_{dd} (power supply) to "V_{out}". Likewise, when the p-MOS is on, the n-MOS is off, limiting the current from "V_{out}" to the ground. As such, very little power is consumed since current flow is blocked during the majority of the operation. The only time power is consumed is when both n-MOS and p-MOS are on when the input switches from high to low or vice versa.

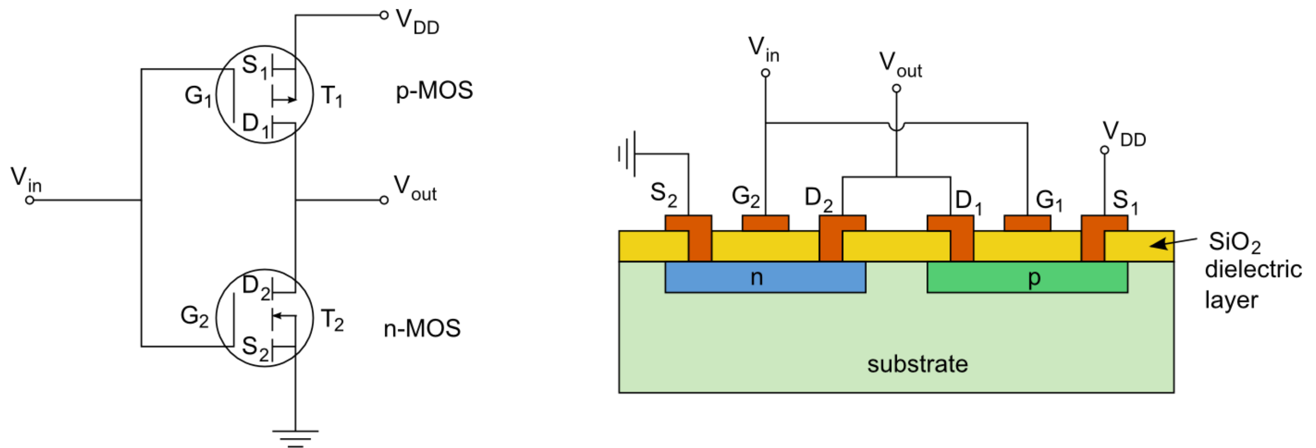

Figure 1-1: CMOS made from an n-type and a p-type MOSFET

Another class of emerging nanoscale devices is nanoelectromechanical systems (NEMS). NEMS are electromechanical systems with submicron critical dimensions. NEMS have the potential to offer superior solutions to many areas including communications, information technology, medical, mechanical, and aerospace technologies as they can attain fundamental frequencies in the microwave range, mechanical quality factors in the tens of thousands, force sensitivities at the attonewton level, active masses in the femtogram range, mass sensitivity at the level of individual molecules, heat capacities far below a yoctocalorie, etc [3]. Although NEMS can be designed using a variety of materials including silicon, silicon carbide, single and multiwall carbon nanotubes, and other materials, silicon is one of the most actively investigated materials for many nanotechnology applications because of its technological importance. High performance NEMS such as nanoswitches [4] and nanoresonators [5] have been fabricated and demonstrated recently as shown in Figure 1-2. Such NEM devices provide tremendous opportunities and enable potential applications in mass memory storage, high-frequency electrical switches, and mass or force sensors.

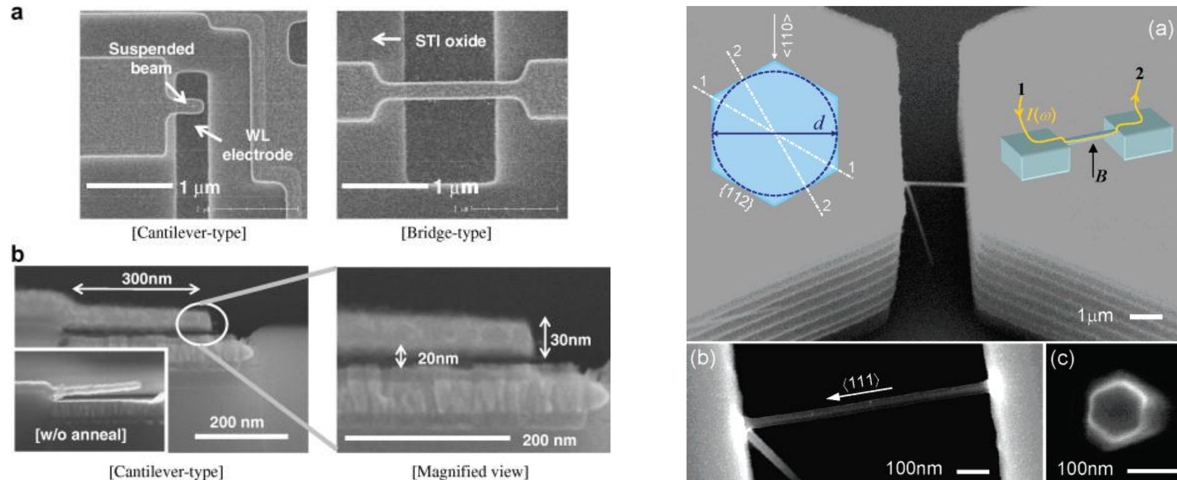

Figure 1-2: Nanoelectromechanical Systems (NEMS). Left: a nanoswitch [4]. Right: an ultra-high frequency nanoresonator [5].

Parallel to the development of nanodevices, in the past decade, synthesis and processing techniques have been developed to create nanostructured materials with highly controlled material composition, structures and related physical properties [6-8]. Examples of the engineered nanostructures include nanotubes, quantum dots, superlattices, thin films and nanocomposites. Nanocomposites are composite materials which incorporate nanosized particles [9] or contain fibers with at least one dimension in the nano-scale [10]. In general, a nanocomposite can be regarded as a solid combining a bulk matrix and nano-scale phases. The phases can be nanoparticles, nanowires, nanoplatelets and etc. The addition of nanosized phases into the bulk matrix can lead to significantly different material properties compared to their macrocomposite counterparts, which include mechanical strength [11,12], toughness, optical properties, electrical conductivity and thermal conductivity [13]. Because of these extraordinary properties, nanocomposites promise new applications in many fields such as ultra-high strength and ultra-light automotive parts [14], nonlinear optics, biomedical applications [15,16], sensors

and actuators [17,18], and thermoelectric devices [19,20]. Figure 1-3 shows two examples of nanostructured materials in sensing and thermoelectric energy conversion applications.

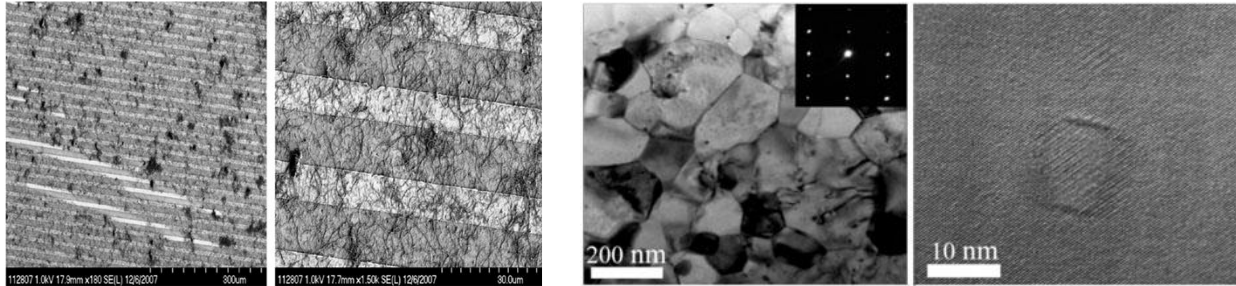

Figure 1-3: Nanostructured materials. Left: nanostructured microsensor [18]. Nanocomposite thermoelectric material [20].

Many of the applications of nanodevices and nanostructured materials described above are enabled, controlled or facilitated by electrical signals. Design and characterization of such devices and materials can be accelerated by using efficient computational tools that incorporate accurate physical models. Modeling and simulation is essential to experimenting with new state-of-the-art devices to determine feasibility for production. In essence, new techniques in modeling and simulation are required to pace with the development of the advent of new technologies. While various design and simulation tools are available for larger electronic devices and materials (critical dimension > 100 nm), they cannot be used for devices with nanoscale features. This is due to the "nano effects" such as defect, surface and quantum effects in nanostructures and nanomaterials. Among these "nano effects", quantum effects are especially important for the development of nanoelectronic devices and materials. The quantum effects arise from the need to treat carriers as waves whereas the classical Boltzmann transport equations (BTE) treated carriers as particles: tunneling, interference and a varying electric field become important issues

to consider when modeling such small devices [21]. Quantum effects become significant or even dominant when the critical size of the device is less than 20 nm, leading to a very different behavior of electrons in these devices. For example, the electron charge distribution is significantly altered in NEMS switches when the thickness of the NEM switch is comparable to the quantum depletion length [3]. In nanocomposite thermoelectric materials, quantum confinement of the electrons in nanoparticles has a significant influence on the electrical conductivity, and consequently the energy conversion efficiency, of the materials [22]. Therefore, quantum effects must be taken into account in the electronic modeling of nanoscale structures, materials and devices.

1.2 Quantum Mechanical Electrostatic and Transport Models

Various computational models and approaches have been developed to include the quantum effects in the analysis of nanostructures. Early models include the charge control and Gummel-Poon models for bipolar junction transistors (BJTs) [23]. These models serve to predict circuit equivalent models of the transistors. In effect, these models approximate the current at the collector, base and emitter based on a common gain. The equations of the currents were obtained from the transport model for BJTs. The advantage of these models is that they are easy to implement and quick calculations can be done to evaluate certain voltage and current parameters. However, these models work well when the transistor size is relatively large. The models fail to incorporate quantum effects that result from the size reduction mentioned above. In addition, these models only focus on currents and voltage ratios at known junctions.

1.2.1 Schrödinger-Poisson Model for Electrostatic Analysis

The use of the Schrödinger-Poisson iteration method has been demonstrated to model the quantum mechanical electrostatic behavior of semiconductor devices such as nanoscale MOSFET [24,25], quantum dots [26] and NEMS [3]. The Schrödinger equation, an eigenvalue problem, is solved to obtain the eigenenergies and wave functions of the system. For most applications, the lowest eigenenergies and corresponding wave functions are kept for the subsequent charge density calculations since they have the greatest impact on the charge distribution. The eigenenergies and wave functions obtained from the Schrödinger equation are used in the Fermi-Dirac calculation to find charge densities. The charge densities are then used in the Poisson equation to compute the electrical potential in the computational domain. The potential is then used in the Schrödinger equation to get an updated set of eigenenergies and wave functions. This process continues until a converged self-consistent solution is found for the potential or charge density. The effective mass Schrödinger equation is in the form of:

$$H\psi_n = -\frac{\hbar^2}{2m_x^*}\frac{\partial^2\psi_n}{\partial x^2} - \frac{\hbar^2}{2m_y^*}\frac{\partial^2\psi_n}{\partial y^2} - \frac{\hbar^2}{2m_z^*}\frac{\partial^2\psi_n}{\partial z^2} + U(V_h, e\phi)\psi_n = E_n\psi_n \quad (1\text{-}1)$$

where H is the Hamiltonian operator, ψ_n is the wave function, E_n is the eigenenergy, $\hbar$ is the reduced Planck constant, m_x^*, m_y^* and m_z^* are the effective masses in x-, y- and z-directions, respectively, U is the potential energy, V_h is the step potential energy at material hetero-junctions, e is the electron charge, and ϕ is the potential in the domain obtained from the Poisson equation, which is given by

$$\nabla \cdot (\epsilon \nabla \phi) = -q[-n(\phi) + p(\phi) + N_D^+ - N_A^-] \quad (1\text{-}2)$$

where ϵ is the dielectric permittivity, q is the magnitude of the electron charge, n and p are the electron and hole density, respectively, and N_D^+ and N_A^- are the ionized donor and acceptor concentration, respectively. As both the Schrödinger and Poisson equations are second order partial differential equations (PDEs), standard numerical methods such as the finite difference method (FDM) and finite element method (FEM) can be employed straightforwardly to obtain the eigenenergies, wave functions, charge densities and potential. In both FDM and FEM, the computational domain is first discretized into a set of grid points or elements. The governing equations are then discretized over the grid points and elements. One clear advantage to the FDM or FEM is the use of a common discretization for both Schrödinger and Poisson equations, resulting in an efficient computation process. Numerical results obtained can be used to evaluate the complete charge density and potential profile of the device, which is another advantage over the Gummel-Poon and charge control models which only find voltages at certain specified locations.

1.3.2 Schrödinger Poisson Model for Electron Transport Analysis

The electrostatic Schrödinger-Poisson iteration method assumes the electrostatic equilibrium in the device and ignores the contributions from the current carrying leads of the structure. In other words, the aforementioned method is a closed boundary method computing the standing waves in the device, ignoring the solutions that extend to the input and output current carrying leads. To model both the current carrying states that are comprised of solutions in a device region and the current carrying lead region, a quantum transmitting boundary formulation was proposed [27,28]. In essence the quantum transmitting boundary method (QTBM) can be thought of as an extension of the Schrödinger-Poisson method with traveling plane wave open boundary

conditions applied at the leads. In the QTBM, the standing wave solution is decomposed into "sine" and "cosine" modes. The Schrödinger equation must be solved twice, once for the standing waves and once for the traveling waves. The charge density is calculated by using the traveling wave functions and the standing wave eigenenergies. The Poisson equation remains the same, with slight modifications when charge neutrality conditions are considered.

1.3.3 Nonequilibrium Green's Function Method for Electron Transport Analysis

Another popular formulation for numerical electron transport analysis is the nonequilibrium Green's function approach (NEGF) [29,30]. Like QTBM, NEGF approach is capable of modeling ballistic transport of electrons in nanostructures. In NEGF, as opposed to the Schrödinger-Poisson approach, Green's function, which is a response of the system to a given perturbation, must be calculated. In addition, instead of coping with the open boundary conditions, a self-energy matrix is introduced in the NEGF. By composing the Hamiltonian for the entire system, the electron density and current density can be obtained. The expression of the nonequilibrium Green's function is given by [30]:

$$\mathbf{G}(\mathrm{E}) = [\mathrm{E}\mathbf{I} - \widetilde{\mathbf{H}}(\mathrm{x},\mathrm{y}) - \mathbf{\Sigma}_{\mathrm{S}} - \mathbf{\Sigma}_{\mathrm{D}}]^{-1} \tag{1-3}$$

where $\mathbf{G}$ is the Green's function matrix, $\widetilde{\mathbf{H}}$ is the reduced Hamiltonian, E is the energy, $\mathbf{I}$ is the identity matrix, $\mathbf{\Sigma}_{\mathrm{S}}$ and $\mathbf{\Sigma}_{\mathrm{D}}$ are the source and drain contact self-energy matrix, respectively. Once the Green's function is computed for the device, the potential and charge distribution can be calculated from the Green's function. More details of the method can be found in Ref. [29, 30]. Advantages of NEGF include the ability to model open boundary conditions and eliminating the need of solving an eigensystem. The NEGF method has been demonstrated to accurately

simulate the behavior of double-gate MOSFETs [29]. However a major disadvantage to NEGF is the fact that it is computationally intensive, even though it does not solve an eigenvalue problem. In the NEGF method, many intermediate parameters have to be calculated and many linear systems have to be solved before the charge density and potential in the device can be obtained. For devices with large degrees of freedom (DOFs), solving for Green's function can be a tedious and computationally intensive process.

1.3.4 Atomistic Models

When the size of nanodevices reduces further, effective mass approximation of the Hamiltonian may not be valid anymore. Atomistic models are necessary in this case for accurate description of the electron behavior. A popular atomistic model that incorporates the electronic structure of atoms is called the tight binding model [31,32]. The Hamiltonian governing the atomic motions for N_a atoms can be written as [31]:

$$H = \sum_i \frac{P_i^2}{2m} + \sum_n \langle \boldsymbol{\psi}_n | \mathbf{H}_{TB} | \boldsymbol{\psi}_n \rangle + E_{rep} + E_0 N_a \tag{1-4}$$

where the first term is the kinetic energy of the ions, the second term is the electronic potential energy by summing the eigenvalues of n eigenstates from Hamiltonian $\mathbf{H}_{TB}$, E_{rep} is the repulsive potential between ions and E_0 is an energy shift per atom. The tight binding matrix elements are typically constructed from a linear combination of the overlapping atomic orbitals on neighboring atoms [32]. The disadvantage of the tight binding model lies that the model parameters need to be fitted empirically to experimental results. Therefore, the reliability of the model is limited to physical situations which are similar to the experimental conditions under which the parameters were fitted. In addition, the model is typically constructed for interactions

between nearest neighbors only. Care must be taken when the range of interaction between the atoms becomes large.

A type of lower level atomistic modeling methods is the so-called Ab initio methods, typically based on Kohn-Sham density functional theory [33]. Starting with the Schrödinger equation for N non-interacting particles with an effective potential $v_{eff}(r)$:

$$\left(\frac{-\hbar}{2m}\nabla^2 + v_{eff}(r)\right)\psi_i(r) = E_i\psi_i(r) \tag{1-5}$$

where E_i is the energy eigenvalue associated with eigenfunction $\psi_i(r)$. The density can be found as:

$$n(r) = \sum_{i=1}^{N} |\psi_i(r)|^2 \tag{1-6}$$

Since the effective potential is not known in most cases, for a given external potential $v(r)$, the following equation can be used to solve for effective potential:

$$v_{eff}(r) = v(r) - e\varphi(r) + v_{xc}(r) \tag{1-7}$$

where $\varphi(r)$ is the electrostatic potential and $v_{xc}(r)$ is the exchange-correlation potential given by, respectively,

$$\varphi(r) = -e\int dr' \frac{n(r')}{|r - r'|} \tag{1-8}$$

and

$$v_{xc}(r) = \frac{\delta E_{xc}}{\delta n(r)} \tag{1-9}$$

In general, E_{xc} is obtained through a local density approximation and thus $v_{eff}(r)$ can be obtained from a given external potential $v(r)$. Ab initio models are generally considered as the most accurate approaches that are available for device simulations. However, a major disadvantage for this method is the computational cost for a large number of atoms. As such, the method is limited to small systems of several hundred atoms. Recently, however, new methods have been proposed to handle large systems, with the number of operations that scale linear with the size of the system [34].

1.4 Motivation of CMS based Approaches

The goal of this research is to develop numerical methods that can accurately and efficiently model the electronic behavior of nanoscale semiconductor devices such as quantum wells and MOSFETs. Among the quantum mechanical models briefly described above, the Schrödinger-Poisson model has its unique advantages. As a continuum model, it can describe the quantum mechanical behavior of electrons in nanostructures with dimensions ranging from several nanometers to several hundred nanometers. Standard numerical methods such as the finite element method can be used to implement the model straightforwardly, enabling the simulation of multi-dimensional devices with complex geometric features. These characteristics make the Schrödinger-Poisson model suitable for the computational analysis of quantum wells and MOSFETs. However, numerical solution of the Schrödinger-Poisson model can be expensive when the degrees of freedom (DOF) of the system are large. The main computational cost occurs in solving the discretized Schrödinger equation which is an eigenvalue problem with its

dimension equal to the DOF of the system. Depending on the numerical method employed, the computation cost of solving the eigenvalue problem is in the order of $n^2 \log n \sim n^3$, where n is the DOF of the system. Therefore, reducing the computational cost of solving the Schrödinger equation can largely accelerate the simulation process of nanodevices.

In this research, we propose a component mode synthesis (CMS) approach to reduce the computational cost of the numerical solution of the Schrödinger equation. CMS was originally developed as a modal order reduction method in solving large mechanical systems [35-37]. In the mechanical analysis using CMS, the large mechanical system is discretized into components and the component modes are calculated individually. A small set of component modes were retrained to construct a set of Ritz basis vectors. In this work, the CMS approach is extended in the Schrödinger-Poisson quantum mechanical electrostatic and transport analysis where a set of basis vectors are constructed to approximate the wave functions in each component. The global energy levels and wave functions are then recovered by the synthesis of these component wave functions. Different from mechanical analysis where only a few vibrational modes are sufficient to model the dynamic response, in some cases, it is necessary to calculate many energy levels and wave functions in order to compute the charge concentrations accurately. In addition to reducing the dimensions of the system, the procedure is fairly simple to implement. In addition, the accuracy can be tuned by adjusting the number of modes retained. If all modes are kept, the CMS solution is exactly the same as the solution obtained by solving the full eigensystem. This characteristic can be used to verify the correctness of the CMS implementation. The reduction of computational cost is crucial as the solution of the Schrödinger equation is present in both the electrostatic and electron transport analyses. In this thesis, the CMS approach is applied to

compute the electrostatic and transport properties of a set of semiconductor devices including a quantum wire and several multiple-gate MOSFETs.

The rest of the thesis is organized as follows. Chapter 2 describes the CMS approach for solving the Schrödinger equation; the self-consistent numerical solution of Schrödinger-Poisson equations for electrostatic analysis is presented in Chapter. 3; the CMS based Quantum Transmitting Boundary Method (QTBM) for electron transport analysis is presented in Chapter 4; and Chapter 5 presents the conclusions.

Chapter 2 Component Mode Synthesis (CMS) Approach for Solving the Schrödinger Equation

2.1 Effective Mass Schrödinger Equation and Its Finite Element Formulation

As discussed in Chapter 1, the 3-D Schrödinger equation is given by

$$H\psi_n = -\frac{\hbar^2}{2m_x^*}\frac{\partial^2\psi_n}{\partial x^2} - \frac{\hbar^2}{2m_y^*}\frac{\partial^2\psi_n}{\partial y^2} - \frac{\hbar^2}{2m_z^*}\frac{\partial^2\psi_n}{\partial z^2} + U(V_h, e\phi)\psi_n = E_n\psi_n \tag{2-1}$$

where H is the Hamiltonian, U is the potential energy, m_x^* and m_y^* are the effective electron or hole mass in the x- and y-direction, respectively, ψ_n and E_n are the eigenpairs to be solved where n denotes the n-th of eigenstates. V_h is the energy difference at the heterojunction due to the band offset caused by two different materials. For many practical devices, the Schrödinger equation can be simplified to its 2-D version, i.e., the solution of the Schrödinger equation does not vary in the z-direction. This approximation can be justified due to the geometry of a quantum well, a 2-D device. For the MOSFET, this approximation is also valid since the cross-section of the MOSFET does not change in the z-direction. The 2-D Schrödinger equation can be written as

$$H\psi_n = -\frac{\hbar^2}{2m_x^*}\frac{\partial^2\psi_n}{\partial x^2} - \frac{\hbar^2}{2m_y^*}\frac{\partial^2\psi_n}{\partial y^2} + U(V_h, e\phi)\psi_n = E_n\psi_n \tag{2-2}$$

We employ the finite element method (FEM) to solve the 2-D Schrödinger equation. The process of FEA involves the transformation of the governing equation into an integral (weak) form. The domain is subsequently discretized into elements. On each element, the weak form equation is approximated by using the finite element shape functions to form local matrices and

vectors. The integrals in the integral equation are then evaluated through Gaussian quadrature [38]. Afterwards, the local matrices and vectors are then assembled into a global system of equations to be solved using a linear solver. The weak form of the Schrödinger equation, derived by Galerkin's method of weighted residuals, is given as:

$$-\int_{\Gamma} \delta\psi_n \frac{\hbar^2}{2} (\mathbf{M}^{-1}\nabla\psi_n) \cdot \hat{\mathbf{n}} + \int_{\Omega} \frac{\hbar^2}{2} (\nabla\delta\psi_n) \cdot \mathbf{M}^{-1}(\nabla\psi_n) d\Omega + \int_{\Omega} (\delta\psi_n)(U - E_n)(\psi_n) d\Omega = 0 \tag{2-3}$$

where $\hat{\mathbf{n}}$ is the unit normal vector to the surface (or domain boundary) Γ. In electrostatic analysis, the wave functions are zero on the boundary of the device. Therefore, the first boundary term $\int_{\Gamma} \ldots d\Gamma$ equals to zero since $\delta\psi_n = 0$ on the closed boundary. The diagonal inverse effective mass matrix $\mathbf{M}^{-1}$ is defined for each element as

$$\mathbf{M}^{-1} = \begin{bmatrix} 1/m_x^* & 0 \\ 0 & 1/m_y^* \end{bmatrix} \tag{2-4}$$

In our implementation, 4-node linear quadrilateral elements are used to discretize the device domain. Within each element, the unknown wave function and its variation are approximated as

$$\boldsymbol{\psi}_n = [N_1 \quad N_2 \quad N_3 \quad N_4] \begin{bmatrix} \psi_{n1} \\ \psi_{n2} \\ \psi_{n3} \\ \psi_{n4} \end{bmatrix} \qquad \delta\boldsymbol{\psi}_n = [N_1 \quad N_2 \quad N_3 \quad N_4] \begin{bmatrix} \delta\psi_{n1} \\ \delta\psi_{n2} \\ \delta\psi_{n3} \\ \delta\psi_{n4} \end{bmatrix} \tag{2-5}$$

Their derivatives are then given by

$$\nabla\boldsymbol{\psi}_n = \begin{bmatrix} \frac{\partial N_1}{\partial x} & \frac{\partial N_2}{\partial x} & \frac{\partial N_3}{\partial x} & \frac{\partial N_4}{\partial x} \\ \frac{\partial N_1}{\partial y} & \frac{\partial N_2}{\partial y} & \frac{\partial N_3}{\partial y} & \frac{\partial N_4}{\partial y} \end{bmatrix} \begin{bmatrix} \psi_{n1} \\ \psi_{n2} \\ \psi_{n3} \\ \psi_{n4} \end{bmatrix} \qquad \nabla\delta\boldsymbol{\psi}_n = \begin{bmatrix} \frac{\partial N_1}{\partial x} & \frac{\partial N_2}{\partial x} & \frac{\partial N_3}{\partial x} & \frac{\partial N_4}{\partial x} \\ \frac{\partial N_1}{\partial y} & \frac{\partial N_2}{\partial y} & \frac{\partial N_3}{\partial y} & \frac{\partial N_4}{\partial y} \end{bmatrix} \begin{bmatrix} \delta\psi_{n1} \\ \delta\psi_{n2} \\ \delta\psi_{n3} \\ \delta\psi_{n4} \end{bmatrix} \tag{2-6}$$

where N_1, N_2, N_3 and N_4 are the shape functions. An arbitrary quadrilateral element is mapped onto a square master element as shown in Figure 2-1. The shape functions are defined on the master element as:

$$N_1 = \frac{1}{4}(1+\xi)(1+\eta) \qquad N_2 = \frac{1}{4}(1-\xi)(1+\eta) \tag{2-7}$$

$$N_3 = \frac{1}{4}(1-\xi)(1-\eta) \qquad N_4 = \frac{1}{4}(1+\xi)(1-\eta) \tag{2-8}$$

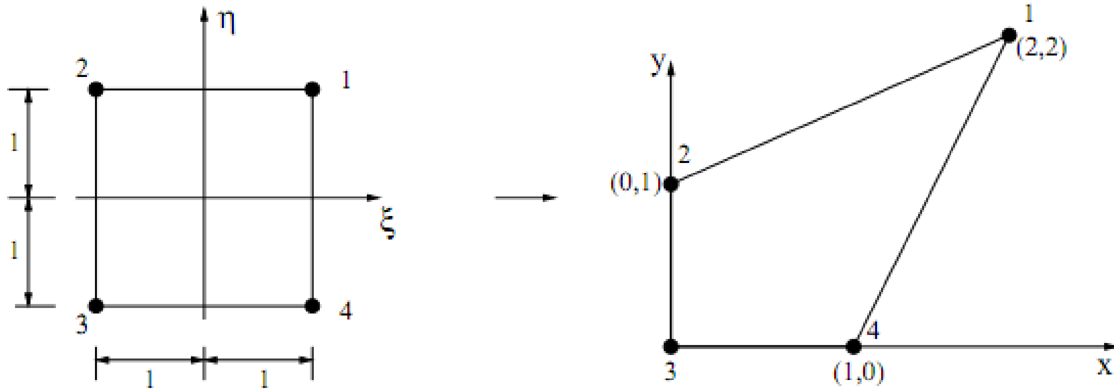

Figure 2-1: An example of isoparametric mapping of 4-node linear quadrilateral elements.

The derivatives of the shape functions defined on the master element are mapped to arbitrary quadrilateral element as

$$\begin{bmatrix} \frac{\partial N_i}{\partial x} & \frac{\partial N_i}{\partial y} \end{bmatrix} = \begin{bmatrix} \frac{\partial N_i}{\partial \xi} & \frac{\partial N_i}{\partial \eta} \end{bmatrix} \mathbf{J}^{-T} \qquad i = 1, 2, 3, 4 \tag{2-9}$$

where **J** is the Jacobian matrix given by

$$\mathbf{J} = \begin{bmatrix} \frac{\partial x}{\partial \xi} & \frac{\partial y}{\partial \xi} \\ \frac{\partial x}{\partial \eta} & \frac{\partial y}{\partial \eta} \end{bmatrix} \tag{2-10}$$

Substituting the approximations given in Eqs. (2-5, 2-6) into the weak form, Eq. (2-3), it can be shown that the weak form can be written as the following matrix form for each element:

$$\mathbf{T}^e \begin{bmatrix} \psi_{n1} \\ \psi_{n2} \\ \psi_{n3} \\ \psi_{n4} \end{bmatrix} + \mathbf{V}^e \begin{bmatrix} \psi_{n1} \\ \psi_{n2} \\ \psi_{n3} \\ \psi_{n4} \end{bmatrix} = E_n \, \mathbf{M}^e \begin{bmatrix} \psi_{n1} \\ \psi_{n2} \\ \psi_{n3} \\ \psi_{n4} \end{bmatrix} \tag{2-11}$$

where matrix $\mathbf{T^e}$ represents the second term in Eq. (2-3), $\mathbf{V^e}$ and $\mathbf{M^e}$ make up the third term in Eq. (2-3). The expressions of the element matrices $\mathbf{T}^e, \mathbf{V}^e$ and $\mathbf{M}^e$ are

$$\mathbf{T}^e = \frac{\hbar^2}{2} \int_{-1}^{1} \int_{-1}^{1} \begin{bmatrix} \frac{\partial N_1}{\partial \xi} & \frac{\partial N_1}{\partial \eta} \\ \frac{\partial N_2}{\partial \xi} & \frac{\partial N_2}{\partial \eta} \\ \frac{\partial N_3}{\partial \xi} & \frac{\partial N_3}{\partial \eta} \\ \frac{\partial N_4}{\partial \xi} & \frac{\partial N_4}{\partial \eta} \end{bmatrix} \mathbf{J}^{-T} \mathbf{M}^{-1} \mathbf{J}^{-1} \begin{bmatrix} \frac{\partial N_1}{\partial \xi} & \frac{\partial N_2}{\partial \xi} & \frac{\partial N_3}{\partial \xi} & \frac{\partial N_4}{\partial \xi} \\ \frac{\partial N_1}{\partial \eta} & \frac{\partial N_2}{\partial \eta} & \frac{\partial N_3}{\partial \eta} & \frac{\partial N_4}{\partial \eta} \end{bmatrix} \det(\mathbf{J}) \, d\xi d\eta \tag{2-12}$$

$$\mathbf{V}^e = \int_{-1}^{1} \int_{-1}^{1} U \begin{bmatrix} N_1 \\ N_2 \\ N_3 \\ N_4 \end{bmatrix} [N_1 \quad N_2 \quad N_3 \quad N_4] \det(\mathbf{J}) \, d\xi d\eta \tag{2-13}$$

$$\mathbf{M}^e = \int_{-1}^{1} \int_{-1}^{1} \begin{bmatrix} N_1 \\ N_2 \\ N_3 \\ N_4 \end{bmatrix} [N_1 \quad N_2 \quad N_3 \quad N_4] \det(\mathbf{J}) \, d\xi d\eta \tag{2-14}$$

where the term $\det(\mathbf{J})$, which can be thought of as an area scaling factor between an element and the master element, is the determinant of the Jacobian matrix given in Eq. (2-10). After all the element matrices are obtained, the global matrices are then constructed through the standard finite element assembly process. The global system is then obtained as

$$(\mathbf{T} + \mathbf{V})\boldsymbol{\psi}_\mathrm{n} = \mathrm{E}_\mathrm{n}\mathbf{M}\boldsymbol{\psi}_\mathrm{n} \tag{2-15}$$

Eq. (2-15) is a generalized eigenvalue problem which can be solved by using standard solvers.

2.2 CMS Method

The general CMS process is composed of four basic steps: discretization of the domain into a discrete number of components, the composition of component basis vectors, the coupling of the components to form a DOF-reduced global system, the solution of the reduced global system assembled to produce the global wave functions. Figure 2-2 shows an example to illustrate the procedure. The meshed device domain is first decomposed into a set of components. Each component contains a number of elements. The portions of the component boundary are categorized into domain boundary or component interface. The eigenvalue problem obtained from the Schrödinger equation is solved in each component. As component DOF is typically much less than the global DOF, the computational cost is small to solve the component eigenvalue problems. Once the component wave functions (or component modes) are calculated, the wave functions in the components are then “synthesized” to produce the global wave functions. The obtained global wave functions and energy levels are used in the calculation of charge density in electrostatic or electron transport analysis, as shown in Figure 2-2.

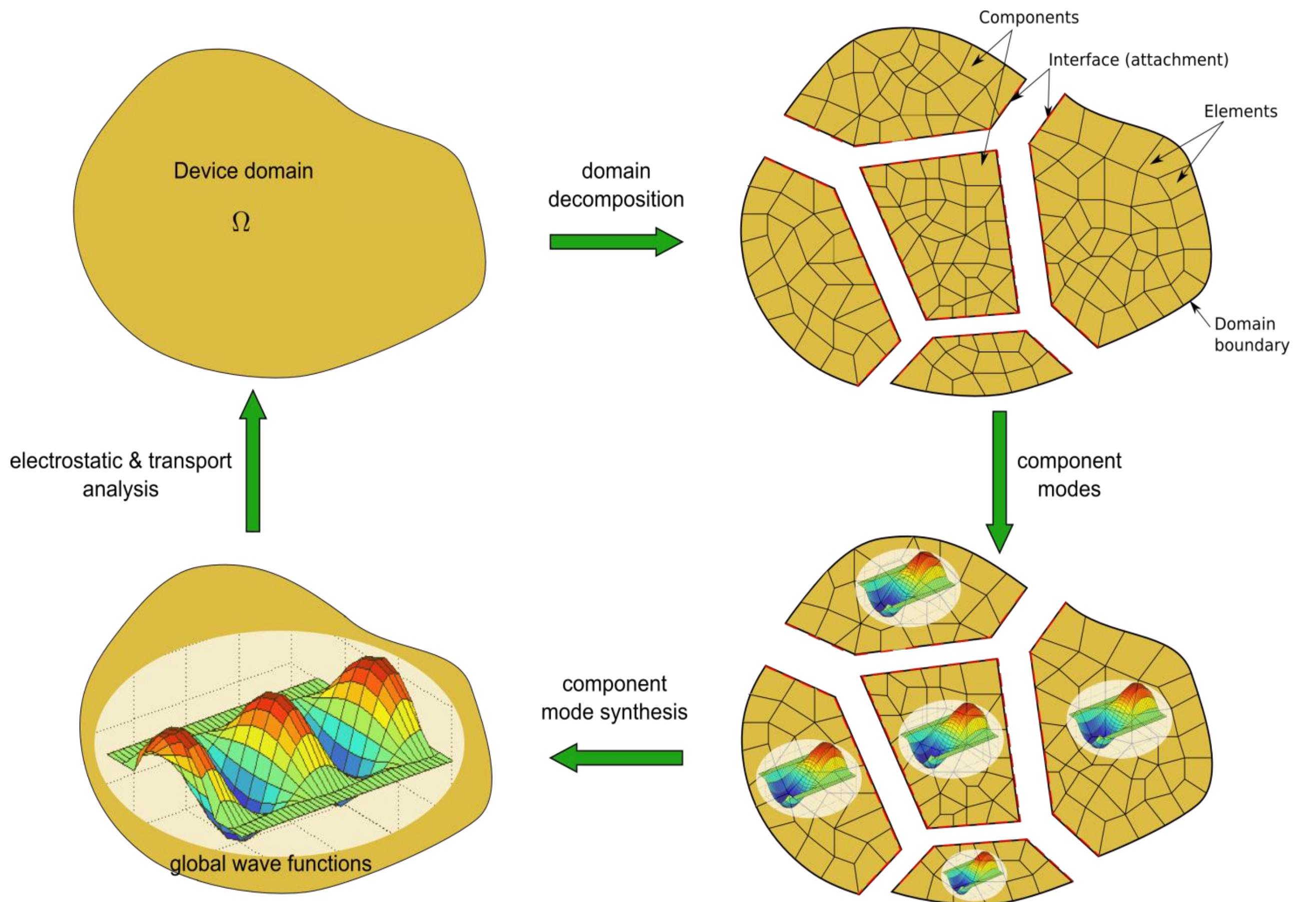

Figure 2-2: Schematic of the component mode synthesis approach for solving the Schrödinger equation.

For each component obtained from the domain decomposition as shown in Figure 2-2, the eigenvalue problem can be denoted as [39]

$$\left(\boldsymbol{\Phi}^{j} - E^{j}\mathbf{M}^{j}\right)\boldsymbol{\psi}^{j} = 0 \qquad\qquad j = 1,2,\ldots,m \tag{2-16}$$

where superscript j denotes the component number and m is the total number of components. $\mathbf{\Phi}^{\mathrm{j}}$ can be assembled from $\mathbf{T}^{\mathrm{e}}$ and $\mathbf{V}^{\mathrm{e}}$ as described in Section 2.1 while $\mathbf{M}^{\mathrm{j}}$ can be assembled from $\mathbf{M}^{\mathrm{e}}$ given in Eq. (2-14). In an electrostatic analysis, the wave function $\boldsymbol{\psi}$ is zero on the domain boundary. As such, the degrees of freedom (DOF) associated with the wave functions on the global boundary can be neglected and discarded. These wave function DOFs are deleted in the implementation. The wave function DOFs in each component, excluding the deleted global boundary DOFs, are separated into attachment and interior parts. By definition, the attachment part contains the wave function DOFs on interface edges which are shared by different components. The interior part contains the wave function DOFs associated with the interior nodes of the component. Note that, in the implementation of this categorization of the DOFs, the global boundary type takes precedence over the attachment type. For example, if a node is both on the global boundary and an interface edge, it is treated as a global boundary node. The attachment and interior DOFs are denoted by subscripts "a" and "i", respectively. With respect to the attachment and interior DOFs, Eq. (2-16) can be partitioned as

$$\left(\begin{bmatrix}\mathbf{\Phi}_{\mathrm{ii}}^{\mathrm{j}} & \mathbf{\Phi}_{\mathrm{ia}}^{\mathrm{j}}\\ \mathbf{\Phi}_{\mathrm{ai}}^{\mathrm{j}} & \mathbf{\Phi}_{\mathrm{aa}}^{\mathrm{j}}\end{bmatrix} - \mathrm{E}^{\mathrm{j}}\begin{bmatrix}\mathbf{M}_{\mathrm{ii}}^{\mathrm{j}} & \mathbf{M}_{\mathrm{ia}}^{\mathrm{j}}\\ \mathbf{M}_{\mathrm{ai}}^{\mathrm{j}} & \mathbf{M}_{\mathrm{aa}}^{\mathrm{j}}\end{bmatrix}\right)\begin{bmatrix}\boldsymbol{\psi}_{\mathrm{i}}^{\mathrm{j}}\\ \boldsymbol{\psi}_{\mathrm{a}}^{\mathrm{j}}\end{bmatrix} = \begin{bmatrix}\mathbf{0}\\ \mathbf{0}\end{bmatrix} \tag{2-17}$$

The attachment DOFs are then fixed such that $\boldsymbol{\psi}_{\mathrm{a}}^{\mathrm{i}} = 0$ and thus the following equation is obtained from Eq. (2-17):

$$\left(\mathbf{\Phi}_{\mathrm{ii}}^{\mathrm{i}} - \mathrm{E}^{\mathrm{j}}\mathbf{M}_{\mathrm{ii}}^{\mathrm{j}}\right)\boldsymbol{\psi}_{\mathrm{i}}^{\mathrm{j}} = 0 \tag{2-18}$$

From Eq. (2-18), the eigenpairs ($\mathrm{E}^{\mathrm{j}}, \boldsymbol{\psi}_{\mathrm{i}}^{\mathrm{j}}$) can be computed for a component j. In CMS, a small set of eigenpairs are retained corresponding to the lowest energies from Eq. (2-18) and assembled

into a component modal matrix $\widehat{\mathbf{D}}_{\mathrm{i}}^{\mathrm{j}}$. Our implementation uses both the maximum number of eigenpairs possible and the option of a set value. The option of having the maximum number of retained eigenpairs is included for implementation verification. In device simulations, however, it is not necessary to include all eigenpairs but rather a small set with respect to the total number of interior DOFs to achieve sufficient accuracy. The component modal matrix is given by

$$\widehat{\mathbf{D}}_{\mathrm{i}}^{\mathrm{j}} = \begin{bmatrix} \boldsymbol{\psi}_{\mathrm{i1}}^{\mathrm{j}} & \boldsymbol{\psi}_{\mathrm{i2}}^{\mathrm{j}} & \cdots & \boldsymbol{\psi}_{\mathrm{ik}}^{\mathrm{j}} \end{bmatrix} \tag{2-19}$$

where k is the number of retained eigenvectors/wave functions. Note that the number k is much less than the number of total interior nodes present in a given component. Subsequently, a constraint modal matrix is obtained by applying $\mathrm{E}^{\mathrm{j}} = 0$ in the component and enforcing a unit wave function along the attachment DOFs in Eq. (2-17), i.e.

$$\begin{bmatrix} \boldsymbol{\Phi}_{\mathrm{ii}}^{\mathrm{j}} & \boldsymbol{\Phi}_{\mathrm{ia}}^{\mathrm{j}} \\ \boldsymbol{\Phi}_{\mathrm{ai}}^{\mathrm{j}} & \boldsymbol{\Phi}_{\mathrm{aa}}^{\mathrm{j}} \end{bmatrix} \begin{bmatrix} \mathbf{X}_{\mathrm{i}}^{\mathrm{j}} \\ \mathbf{I}_{\mathrm{a}} \end{bmatrix} = \begin{bmatrix} 0 \\ \mathbf{R}_{\mathrm{a}}^{\mathrm{j}} \end{bmatrix} \tag{2-20}$$

where each column of the identity matrix $\mathbf{I}_{\mathrm{a}}$ is used to enforce wave function with unit magnitude at the corresponding attachment DOF while the wave functions of the other attachment node DOF is fixed to zero. $\mathbf{R}_{\mathrm{a}}^{\mathrm{j}}$ is the resulting boundary reaction at the attachment DOFs. As such, the expression for the constraint modal matrix $\mathbf{X}_{\mathrm{i}}^{\mathrm{j}}$ associated with the interior DOFs can be obtained by

$$\mathbf{X}_{\mathrm{i}}^{\mathrm{j}} = -(\boldsymbol{\Phi}_{\mathrm{ii}}^{\mathrm{j}})^{-1}\boldsymbol{\Phi}_{\mathrm{ia}}^{\mathrm{j}} \tag{2-21}$$

Once the matrices $\widehat{\mathbf{D}}_{\mathrm{i}}^{\mathrm{j}}$, $\mathbf{X}_{\mathrm{i}}^{\mathrm{j}}$ are obtained, the component wave functions can then be calculated by

$$\boldsymbol{\psi}^j = \begin{bmatrix} \boldsymbol{\psi}_i^j \\ \boldsymbol{\psi}_a^j \end{bmatrix}_{nx1} = \begin{bmatrix} \widehat{\mathbf{D}}_i^j & \mathbf{X}_i^j \\ \mathbf{0}_a & \mathbf{I}_a \end{bmatrix}_{nxr} \begin{bmatrix} \mathbf{z}_i^j \\ \boldsymbol{\psi}_a^j \end{bmatrix}_{rx1} \tag{2-22}$$

where n is the total component DOFs, and r is the sum of the retained components and attachments DOFs. $\mathbf{I}_a$ and $\mathbf{0}_a$ are the identity and zero matrices associated with the corresponding attachment node, respectively. The vector $\begin{bmatrix} \mathbf{z}_i^j \\ \boldsymbol{\psi}_a^j \end{bmatrix}$ is the generalized coordinate vector. Eq. (2-22) can be written in short form as

$$\boldsymbol{\psi}^j = \mathbf{T}^j \mathbf{z}^j \tag{2-23}$$

where $\mathbf{T}^j$ is referred to as the transformation matrix of component j. Eq. (2-23) shows that the wave functions of component j can be approximated as a linear combination of the column vectors of $\mathbf{T}^j$ with the elements of vector $\mathbf{z}^j$ as the coefficients. In other words, the column vectors of $\mathbf{T}^j$ serve as the basis vectors of component j. Furthermore, since k<< interior DOFs, r<<n. This reduction of modes enables CMS to greatly reduce the computational cost of calculating both component and global wave functions. On the other hand, this reduction of modes introduces an approximation error as well. The solution is only an approximation since only k eigenpairs are retained. The solution is exact only when the number of retained eigenpairs is equal to the total number of interior DOFs. Substituting Eq. (2-23) into Eq. (2-18), we obtain

$$\left(\boldsymbol{\Phi}^j - \mathrm{E}^j \mathbf{M}^j\right) \mathbf{T}^j \mathbf{z}^j = \mathbf{0} \tag{2-24}$$

Multiplying by the transpose of $\mathbf{T}^j$ to both side of Eq. (2-24) gives

$$\left(\mathbf{T}^j\right)^T \left(\boldsymbol{\Phi}^j - \mathrm{E}^j \mathbf{M}^j\right) \mathbf{T}^j \mathbf{z}^j = \mathbf{0} \tag{2-25}$$

Eq. (2-25) can be written in short form as

$$\left(\bar{\boldsymbol{\Phi}}^{\mathrm{j}} - \mathrm{E}^{\mathrm{j}}\bar{\mathbf{M}}^{\mathrm{j}}\right)\mathbf{z}^{\mathrm{j}} = \mathbf{0} \tag{2-26}$$

where

$$\bar{\boldsymbol{\Phi}}^{\mathrm{j}} = \left(\mathbf{T}^{\mathrm{j}}\right)^{\mathrm{T}}\boldsymbol{\Phi}^{\mathrm{j}}\mathbf{T}^{\mathrm{j}} \qquad \bar{\mathbf{M}}^{\mathrm{j}} = \left(\mathbf{T}^{\mathrm{j}}\right)^{\mathrm{T}}\mathbf{M}^{\mathrm{j}}\mathbf{T}^{\mathrm{j}} \tag{2-27}$$

are the reduced matrices for component j. Subsequently, the matrices are assembled into a global modal system via the standard finite element assembly process to find the solution of $\hat{\mathbf{z}}$:

$$\left(\widehat{\boldsymbol{\Phi}} - \mathrm{E}\widehat{\mathbf{M}}\right)\hat{\mathbf{z}} = 0 \tag{2-28}$$

where $\widehat{\boldsymbol{\Phi}}$ and $\widehat{\mathbf{M}}$ represent the global matrices assembled from of $\bar{\boldsymbol{\Phi}}^{\mathrm{j}}$ and $\bar{\mathbf{M}}^{\mathrm{j}}$, respectively. The global wave functions can be recovered by

$$\boldsymbol{\Psi} = \widehat{\mathbf{T}}\hat{\mathbf{z}} \tag{2-29}$$

where $\widehat{\mathbf{T}}$ represents the global assembled transformation matrix of the assembled $\mathbf{T}^{\mathrm{j}}$ matrices.

The fixed-interface CMS approach has several advantages. First of all, the approach has a relatively simple procedure for computing the basis vectors used in the transformation matrix. Additionally, the approach has a straightforward implementation of coupling of components to form the global modal system. Finally, the approach produces high accuracy in the computation of the low eigenvalues and the corresponding eigenvectors.

2.3 Numerical Results

The first numerical example shown in this section is the solution of the Schrödinger equation for a double-gate MOSFET. The dimensions and physical properties of the MOSFET are shown in Figure 2-3. As will be discussed in Chapter 4, the Schrödinger equation is to be solved over the device domain for "cosine" and "sine" modes. The "cosine" and "sine" modes differ in their boundary conditions. For the "sine" mode, the current carrying lead nodes are assigned a Dirichlet boundary condition while the same nodes on the leads are assigned a natural boundary condition for the "cosine" mode. In this section, the CMS solutions of the Schrödinger equation are compared to the direct solutions of the full eigensystem. The device domain is discretized into 40 by 10 elements. In the CMS solution, the mesh is further decomposed into 4 by 5 components with 10 by 2 elements in each component. The first 5 eigenpairs are retained in each component. Table 2-1 shows the comparison of the eigenenergies obtained from the direct and CMS approaches. Figure 2-4 shows the comparison of the "cosine" mode wave functions obtained by using the direct and CMS approaches. It should be noted that wave functions shown are calculated in the first iteration of device simulation, with initial condition of 0V on the domain.

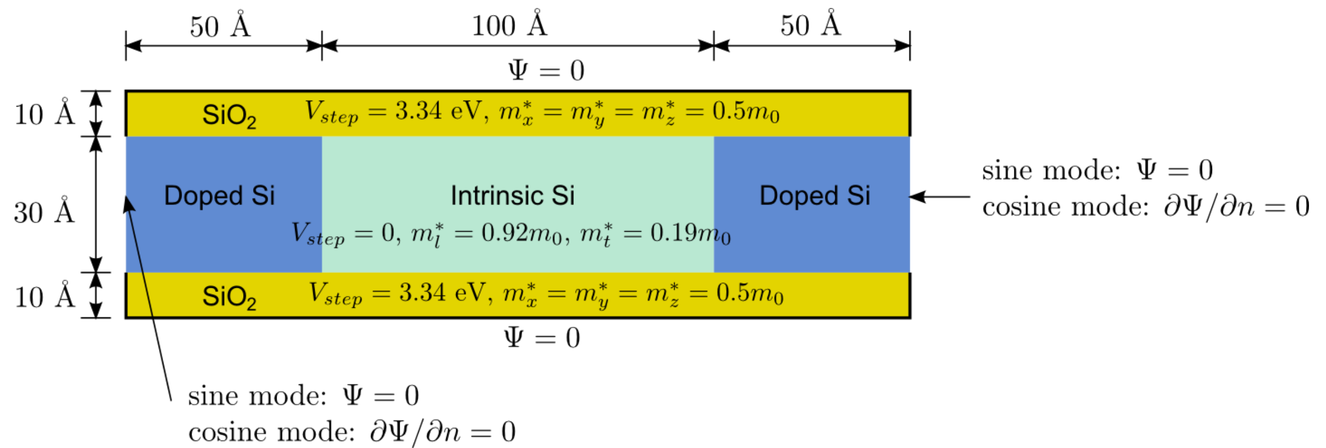

Figure 2-3: Computational domain of a double gate MOSFET.

Table 2-1: Comparison of eigenenergies obtained from the CMS and direct approaches

Direct Esin (eV)	CMS Esin (eV)	Direct Ecos (eV)	CMS Ecos (eV)
0.157682733371887	0.157927834442041	0.157330723099336	0.157544761897325
0.160599364355327	0.161060945206333	0.159276642767386	0.159597734177530
0.165480343803728	0.166291738177092	0.162751702463985	0.163244187447445
0.172355688262674	0.173481584085488	0.167949927883989	0.168706046009338
0.181267665576055	0.183140937278616	0.175013186427522	0.176407598345969

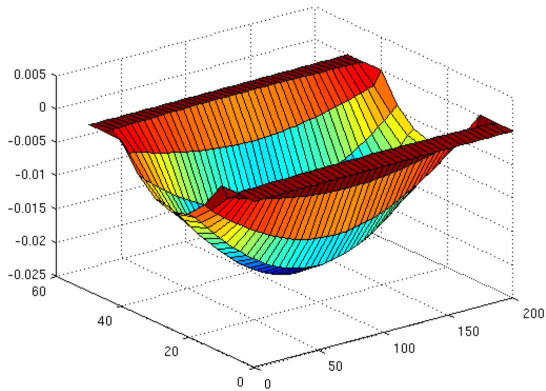

(a)

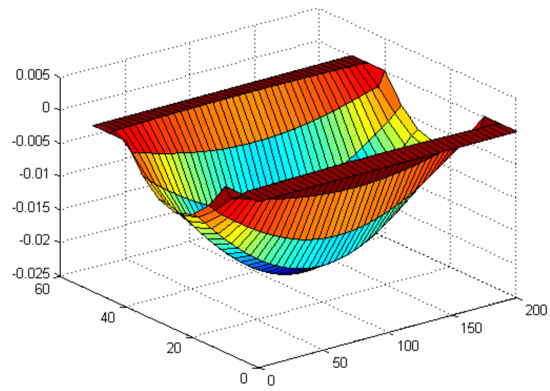

(b)

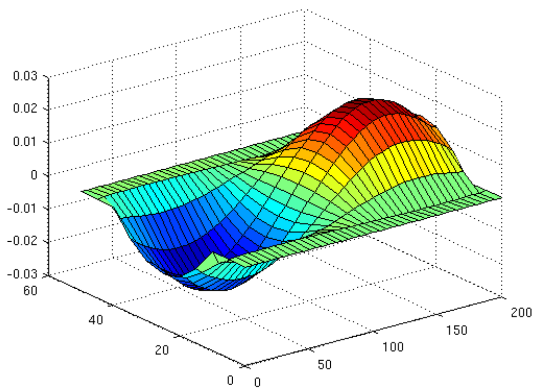

(c)

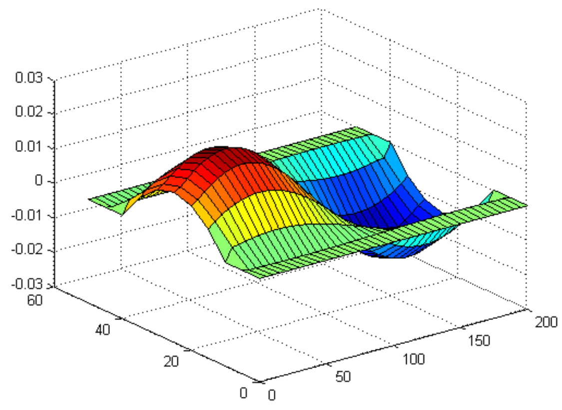

(d)

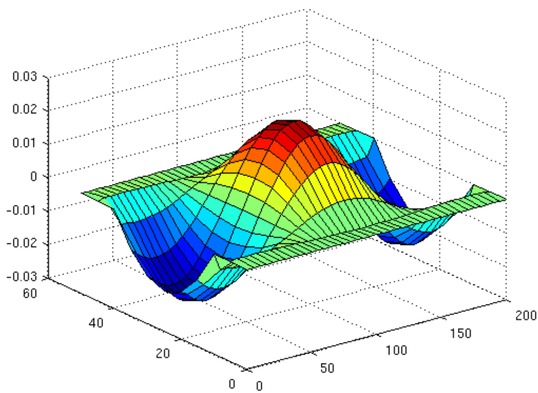

(e)

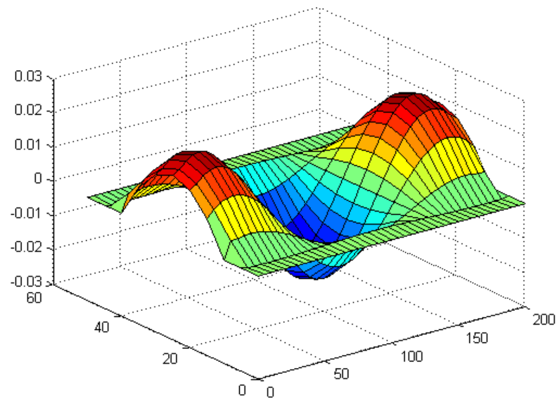

(f)

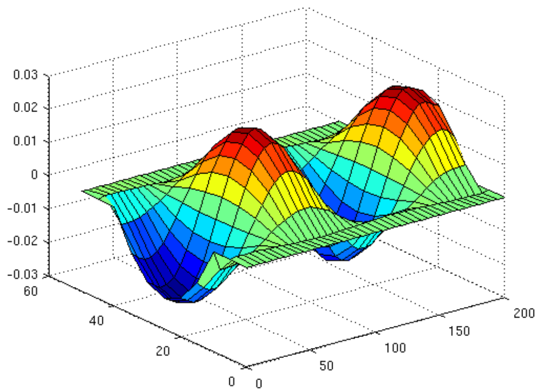

(g)

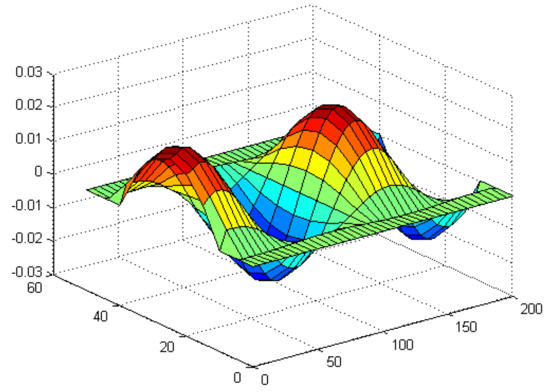

(h)

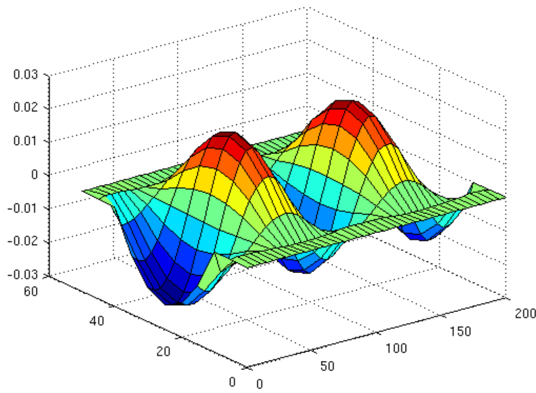

(i)

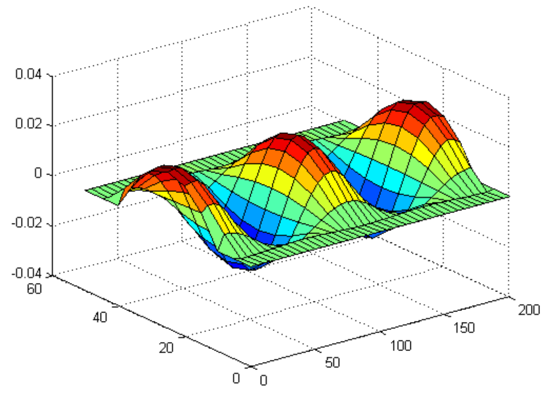

(j)

Figure 2-4: "Cosine" mode wave function solutions for the MOSET. Left column: direct solutions of the full eigensystem. Right column: CMS solutions. Top to bottom: 1st to 5th wave functions. 40 by 10 mesh domain.

From Table 2-1 and Figure 2-4, it is clear that the CMS approach gives quite accurate eigenvalues even when only 5 eigenpairs are retained in each component. The "cosine" mode global wave functions are accurately recovered by the CMS approach. Similar results are obtained for the "sine" mode wave functions. For the sake of brevity, the "sine" mode wave functions are not shown here. One peculiarity that can be seen from Figure 2-4 lies in the fact that the wave functions from the direct and CMS results sometimes have opposite signs. This peculiarity is trivial, as the square of the wave functions form the probability factor necessary in calculating charge density and thus the sign of the wave functions do not contribute to any change in charge density calculations. It is shown from the results that the "sine" and "cosine" modes mirror the behavior of "sine" and "cosine" waves in the x-y plane. There is an offset in the waves due to the contributions of the electron effective masses in the x- and y-directions so the peaks and zeroes do not correspond exactly at the boundaries for the "cosine" and "sine"

modes, respectively. In addition, the wave functions are naturally suppressed in the oxide regions. This is expected since the change in barrier energy (3.34 eV) suppresses the likelihood of locating any electrons in the oxide regions.

In the CMS implementation of “sine” and “cosine” modes, there are major differences to consider as well. For the “sine” mode, the lead nodes can be treated as boundary nodes, thus excluded from CMS analysis. For the “cosine” mode, the lead boundary nodes must be treated as interior or attachment nodes depending on the configuration. If a lead boundary node lies on a component edge, then it is an attachment node. Otherwise, it should be treated as an interior node. Once this preprocessing differentiation of “sine” and “cosine” modes is taken into account, the same solver can be used to obtain solutions for both modes. In fact, the same solver was used to obtain solutions for meshes of varying sizes as well, demonstrating the flexibility of such an implementation. Lastly, in the preprocessing portion of the implementation, it is necessary to define nodes as interior, attachment and/or global boundary type. There are corner cases where a node can be both an attachment node and a global boundary node. In such cases, the node should be classified as a global boundary node to maintain consistency and produce results consistent with the direct approach.

The second example is a quantum well with a GaAs nanowire embedded in the AlGaAs material. The dimensions and physical properties of the quantum well structure are shown in Figure 2-5. The domain is discretized into 40 by 40 elements. In the CMS calculations, the domain is decomposed into 4 by 4 components with each component having 10 by 10 elements. Homogeneous Dirichlet boundary condition of the wave function is applied on the outer boundary of the quantum well. The step potential energy is 0.276 eV between AlGaAs and

GaAs. Figure 2-6 shows the comparison of the first 5 wave functions obtained by using the direct and CMS approaches.

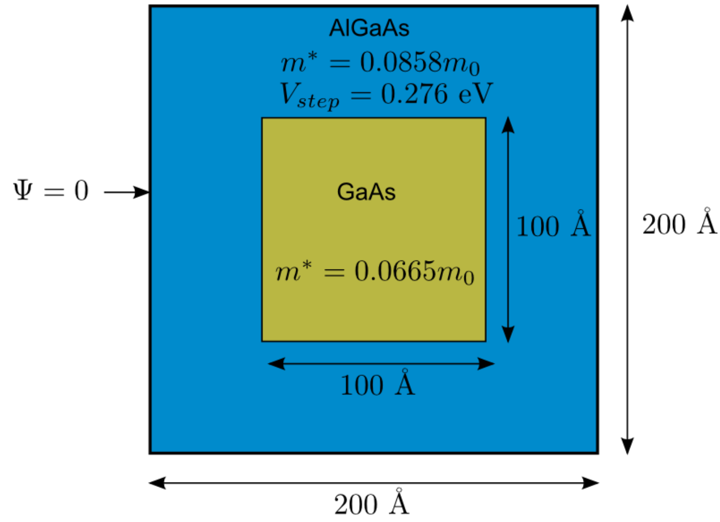

Figure 2-5: computational domain of a quantum wire

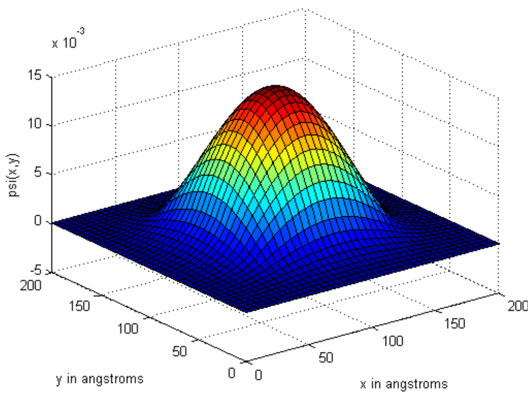

(a)

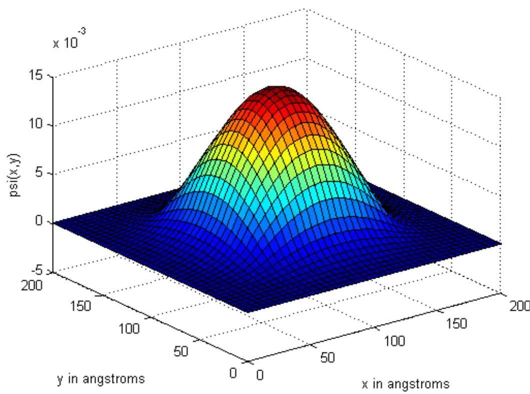

(b)

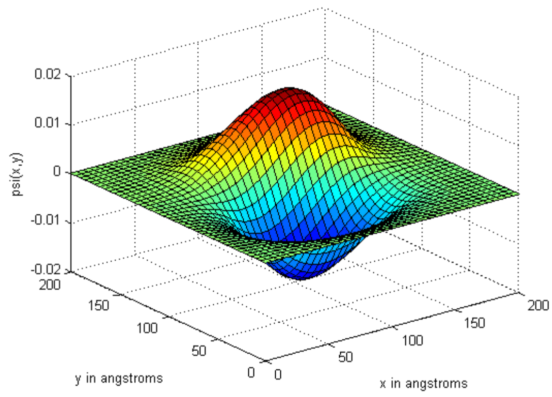

(c)

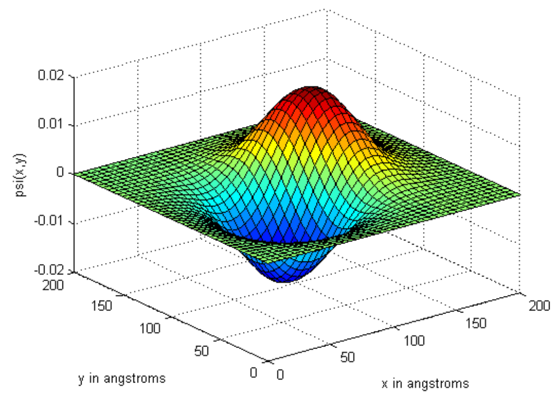

(d)

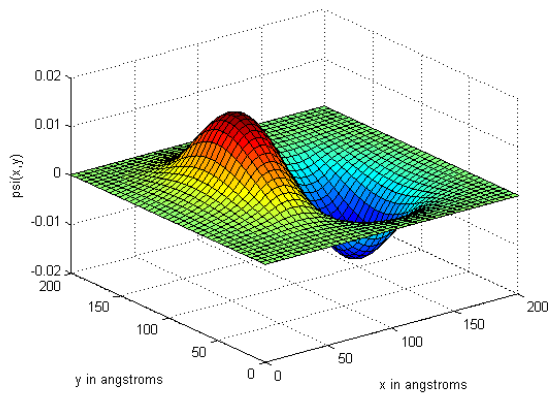

(e)

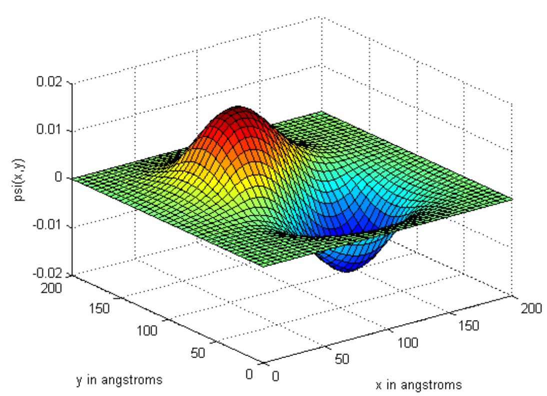

(f)

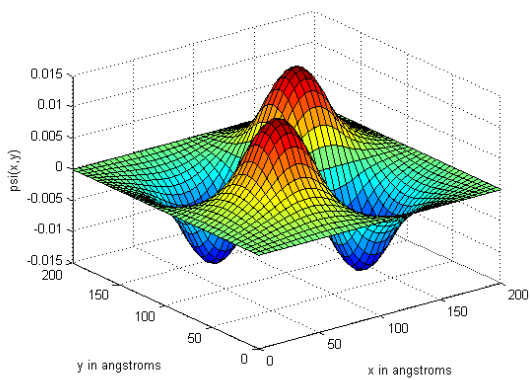

(g)

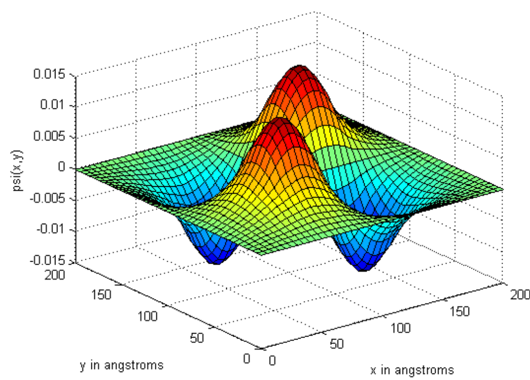

(h)

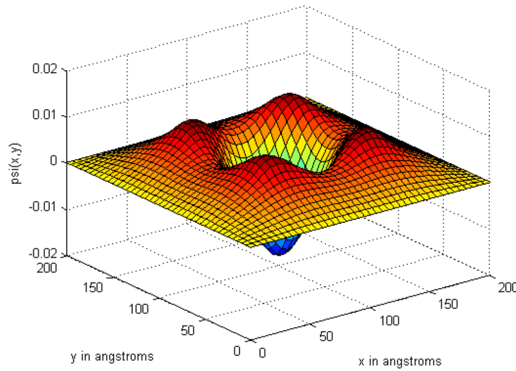

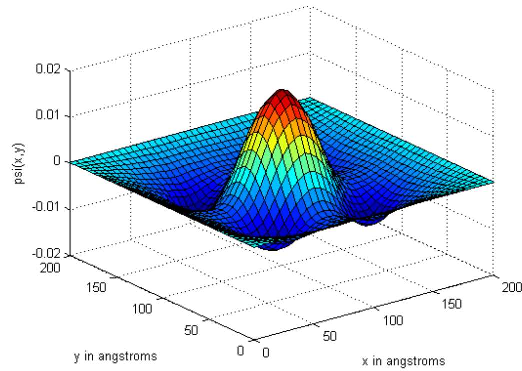

(i) (j)

Figure 2-6: Wave function solutions for the quantum wire. Left column: direct solutions of the full eigensystem. Right column: CMS solutions. Top to bottom: 1st to 5th wave functions. 40 by 40 mesh domain.

Similar to the results shown in the double-gate MOSFET case, the global wave functions are accurately reproduced by using the CMS approach. As demonstrated in the two examples, CMS is a powerful tool that can be successfully used to retain accuracy while reducing the computation cost of solving the Schrödinger equation. In the following chapters, the CMS solutions of the Schrödinger equation are employed in the full Schrödinger-Poisson simulation of a set of nanostructures and nanodevices. Computational cost and accuracy will be compared between the CMS based and the direct Schrödinger-Poisson solvers for these device simulations.

Chapter 3 Quantum Mechanical Electrostatic Analysis of Nanostructures and Nanodevices

3.1 Schrödinger-Poisson Approach and Finite Element Formulation

In the Schrödinger-Poisson method of electrostatic analysis, an iterative procedure is carried out between the Schrödinger and Poisson Equations. The eigenenergies and wave functions obtained from the Schrödinger equation for a given potential profile in the device domain are used in the calculation of the charge density in the domain. The calculated charge density is then used in the Poisson equation to obtain the new potential profile. The updated potential profile is then again applied in the Schrödinger equation to compute the new eigenpairs. This iterative procedure continues until a self-consistent solution between the Schrödinger and Poisson equations is obtained. The CMS based solution approach for the Schrödinger equation has been described in Chapter 2. For the sake of completeness, the global matrix from of the Schrödinger equation is repeated here, i.e.,

$$\boldsymbol{\Phi}\boldsymbol{\psi}_n = E_n \mathbf{M}\boldsymbol{\psi}_n \tag{3-1}$$

Once the eigenpairs $(E_n, \boldsymbol{\psi}_n)$ are computed by using the CMS techniques as described previously, the electron and hole densities can be calculated by

$$n(\phi) = \frac{N_{nd}}{\pi}\left(\frac{2m_{nz}k_B T}{\hbar^2}\right)^{1/2} \times \sum_{n=1}^{\infty} |\psi_n(\phi)|^2 \, \mathcal{F}_{-1/2}\left(\frac{E_F - E_n(\phi)}{k_B T}\right) \tag{3-2}$$

$$p(\phi) = \frac{N_{pd}}{\pi}\left(\frac{2m_{pz}k_B T}{\hbar^2}\right)^{1/2} \times \sum_{n=1}^{\infty} |\psi_n(\phi)|^2 \, \mathcal{F}_{-1/2}\left(\frac{E_n(\phi) - E_F}{k_B T}\right) \tag{3-3}$$

where N_{nd} and N_{pd} are the band degeneracy for electrons and holes, respectively, m_{nz} and m_{pz} are the respective electron and hole effective masses in the z-direction, k_B is the Boltzmann constant, T is the temperature, E_F is the Fermi energy, and $\mathcal{F}_{-1/2}$ is the Fermi-dirac integral of order -1/2, given by [26]

$$\mathcal{F}_k(x) = \frac{1}{\Gamma(k+1)} \int_0^\infty \frac{t^k dt}{e^{t-x}+1}, \qquad k > -1 \tag{3-4}$$

The computed electron and hole densities are then used in the Poisson equation, which is given by

$$\nabla \cdot (\epsilon \nabla \phi) = -q[-n(\phi) + p(\phi) + N_D^+ - N_A^-] \tag{3-5}$$

where ϕ is the unknown potential, ϵ is the dielectric permittivity, q is the magnitude of the electron charge, n and p are the electron and hole density, respectively, and N_D^+ and N_A^- are the ionized donor and acceptor concentration, respectively. Note that, in general, when solving for a particular problem, either hole or electron concentrations can be neglected when the donor and acceptor concentrations are well above the intrinsic level. In this work, as the devices under consideration all have n-type doping ($N_A^- = 0$), the hole density term is neglected. The weak form of the Poisson equation can be obtained by using the Galerkin's weighted residual method as

$$-\int_\Gamma \delta\phi_n \, \epsilon \frac{\partial \phi_n}{\partial \hat{n}} \, d\Gamma + \int_\Omega \epsilon \, (\nabla \delta\phi_n) \cdot (\nabla \phi_n) d\Omega - q \int_\Omega (\delta\phi_n)[N_D^+ - n(\phi)] d\Omega = 0 \tag{3-6}$$

Most devices are insulated electronically except for the regions where potentials are applied. For insulated boundary parts, homogeneous Neumann boundary conditions can be applied, i.e.,

$\frac{\partial \phi_n}{\partial \hat{n}} = 0$. Therefore, the first term in Eq. (3-6) can be neglected. The linear weak form given in Eq. (3-6) can be discretized by using the finite element approximation and Gaussian quadrature. The potential can be computed by solving the discretized system. The Schrödinger-Poisson iterations can continue in this fashion. Unfortunately, it has been demonstrated that the convergence of this simple iteration is very poor [26]. In this work, we adopt a predictor-corrector approach for better convergence of the solution. The predictor-corrector approach uses the potential from the previous outer iteration to predict and correct the next potential within the step of solving the Poisson equation. In this approach, the electron density has a modified form as [26]

$$n(\phi) = \frac{N_{nd}}{\pi}\left(\frac{2m_{nz}k_B T}{\hbar^2}\right)^{1/2} \times \sum_{n=1}^{\infty} \left|\psi_n^k(\phi)\right|^2 \mathcal{F}_{-1/2}\left(\frac{E_F - E_n^k + q(\phi - \phi^k)}{k_B T}\right) \quad (3\text{-}7)$$

where ϕ^k is potential obtained from the previous Schrödinger-Poisson outer iteration and ϕ is the unknown potential to be solved in the current iteration. Similar modification can be made to the hole density as well. Note that the electron density now depends on the unknown potential to be solved in the current iteration. Substituting Eq. (3-7) into the weak form, Eq. (3-6) becomes a nonlinear integral equation. The Newton Raphson method [38] for solving nonlinear equations is employed to find the solution of the potential. By using the finite element approximations as described in Eqs. (2-5~2-9) and the Newton Ralphson method, the discretized element weak form can be written as

$$\mathbf{J}^e \Delta \boldsymbol{\phi}^e = -\mathbf{R}^e \quad (3\text{-}8)$$

where $\mathbf{J}^e$ is the element Jacobian matrix, $\mathbf{R}^e$ is referred to as the element residual vector and $\Delta\boldsymbol{\phi}^e$ is the potential increment to be calculated for the element. The element Jacobian matrix can be obtained as

$$\mathbf{J}^e = \mathbf{K}^e + \mathbf{B}^e \tag{3-9}$$

where

$$\mathbf{K}^e = \epsilon \int_{-1}^{1}\int_{-1}^{1} \begin{bmatrix} \frac{\partial N_1}{\partial \xi} & \frac{\partial N_1}{\partial \eta} \\ \frac{\partial N_2}{\partial \xi} & \frac{\partial N_2}{\partial \eta} \\ \frac{\partial N_3}{\partial \xi} & \frac{\partial N_3}{\partial \eta} \\ \frac{\partial N_4}{\partial \xi} & \frac{\partial N_4}{\partial \eta} \end{bmatrix} \mathbf{J}^{-T}\mathbf{J}^{-1} \begin{bmatrix} \frac{\partial N_1}{\partial \xi} & \frac{\partial N_2}{\partial \xi} & \frac{\partial N_3}{\partial \xi} & \frac{\partial N_4}{\partial \xi} \\ \frac{\partial N_1}{\partial \eta} & \frac{\partial N_2}{\partial \eta} & \frac{\partial N_3}{\partial \eta} & \frac{\partial N_4}{\partial \eta} \end{bmatrix} \det(\mathbf{J})\, d\xi d\eta \tag{3-10}$$

and

$$\mathbf{B}^e = q \int_{-1}^{1}\int_{-1}^{1} \begin{bmatrix} \frac{\partial N_1 n(\phi)}{\partial \phi_1} & \frac{\partial N_1 n(\phi)}{\partial \phi_2} & \frac{\partial N_1 n(\phi)}{\partial \phi_3} & \frac{\partial N_1 n(\phi)}{\partial \phi_4} \\ \frac{\partial N_2 n(\phi)}{\partial \phi_1} & \frac{\partial N_2 n(\phi)}{\partial \phi_2} & \frac{\partial N_2 n(\phi)}{\partial \phi_3} & \frac{\partial N_2 n(\phi)}{\partial \phi_4} \\ \frac{\partial N_3 n(\phi)}{\partial \phi_1} & \frac{\partial N_3 n(\phi)}{\partial \phi_2} & \frac{\partial N_3 n(\phi)}{\partial \phi_3} & \frac{\partial N_3 n(\phi)}{\partial \phi_4} \\ \frac{\partial N_4 n(\phi)}{\partial \phi_1} & \frac{\partial N_4 n(\phi)}{\partial \phi_2} & \frac{\partial N_4 n(\phi)}{\partial \phi_3} & \frac{\partial N_4 n(\phi)}{\partial \phi_4} \end{bmatrix}_{\phi=\phi^h} \det(\mathbf{J})\, d\xi d\eta \tag{3-11}$$

The shape functions, their derivatives and associated Jacobian matrix are defined in Eqs. (2-8~2-10). $\phi_i, i = 1, 2, 3, 4$, are the nodal potentials in an element. Note that the derivatives of the modified electron density with respect to the nodal potentials need to be computed in Eq. (3-11). It is easy to show that the derivatives can be obtained as

$$\left.\frac{\partial n(\phi)}{\partial \phi_i}\right|_{\phi=\phi^h} = \frac{N_{nd}}{\pi}\left(\frac{2m_{nz}k_BT}{\hbar^2}\right)^{1/2}$$

$$\times \sum_{n=1}^{\infty} \left|\psi_n^k(\phi^k)\right|^2 \mathcal{F}_{-3/2}\left(\frac{E_F - E_n^k + q(\phi^h - \phi^k)}{k_BT}\right)\frac{qN_i}{k_BT} \tag{3-12}$$

Note that the Fermi-Dirac integral of order -3/2 in Eq. (3-12) is obtained from the following identity:

$$\frac{d}{dx}\mathcal{F}_k(x) = \mathcal{F}_{k-1}(x) \tag{3-13}$$

For implementation purposes, the Fermi-Dirac integrals are sampled for a known range of the input parameter that encompassed the possible values for electron density in the preprocessing step. A table is created to store the pre-calculated function values for the sampling points. For a given input parameter, the value of the Fermi-Dirac functions is calculated by interpolating between the pre-calculated values stored in the table. This step is done to eliminate the need to calculate the Fermi-Dirac integral on every gauss point for every shape function in every element, saving computational costs. The residual vector in Eq. (3-8) is obtained as

$$\mathbf{R}^e = \mathbf{K}^e \begin{Bmatrix} \phi_1 \\ \phi_2 \\ \phi_3 \\ \phi_4 \end{Bmatrix}^h + q\int_{-1}^{1}\int_{-1}^{1} \begin{bmatrix} N_1 \\ N_2 \\ N_3 \\ N_4 \end{bmatrix} (n(\phi^h)\text{-}N_D^+)\det(\mathbf{J})\, d\xi d\eta \tag{3-13}$$

where the superscript “h” denotes the potential obtained from the previous inner iteration (i.e. the Newton-Raphson iteration) of the Poisson equation. Assembling the element matrices and vectors shown in Eq. (3-8) gives the global system

$$\mathbf{J}\Delta\boldsymbol{\phi} = -\mathbf{R} \tag{3-13}$$

Within each Newton-Raphson iteration, the potential increment is found by solving Eq. (3-13). The potential is updated by

$$\boldsymbol{\phi}^{h+1} = \boldsymbol{\phi}^{h} + \Delta\boldsymbol{\phi} \tag{3-13}$$

The process is repeated until a convergence criterion is satisfied. After the Newton-Raphson iterations converge for the potential, the Schrödinger equation is then updated with the new potential and a new outer iteration begins.

3.2 Numerical Results

In this section, we show the results obtained from the quantum mechanical electrostatic analysis of a quantum well and an all-around MOSFET. The dimensions and physical properties of the quantum well are show in Figure 3-1. The doping density is set to be 10^{18} cm^{-3} in the n-type AlGaAs region. The effective masses of GaAs and AlGaAs are set to be $0.0665m_0$ and $0.0858m_0$, respectively. The heterojunction potential between GaAs and AlGaAs is set as 0.276 eV. The relative dielectric constants are 13.18 and 12.31 for GaAs and AlGaAs, respectively. Dirichlet (potential) boundary conditions of 0.3V and -0.3V are applied to the outer boundary. In the direct solution of the Schrödinger equation, the lowest 10 eigenpairs are computed and found to be sufficient for an accurate solution. For the CMS approach, the domain is further discretized into 4 by 4 components, with 9 component eigenpairs retained in each component (note that this number is far less than the total interior DOFs in each component). The domain mesh is varied between 40 by 40 elements to 200 by 200 elements for the direct and CMS approaches.

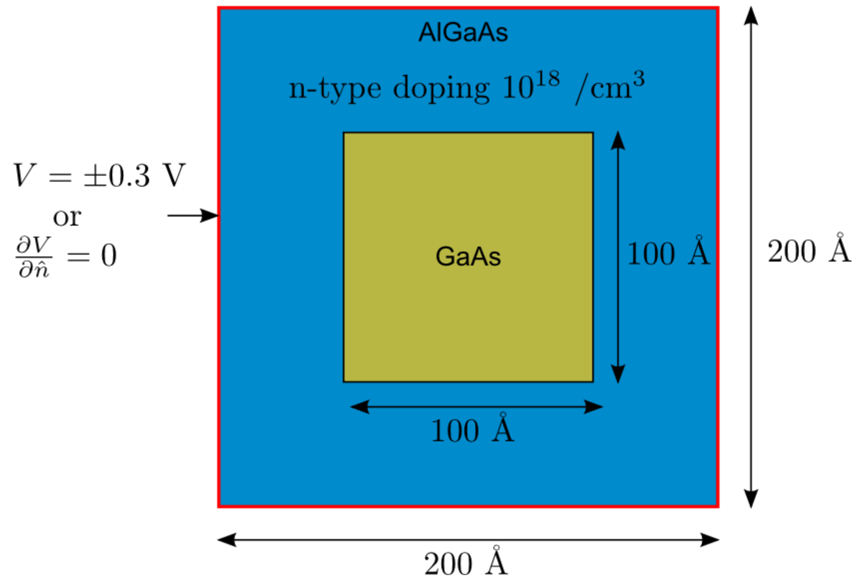

Figure 3-1: Computational domain of a quantum wire.

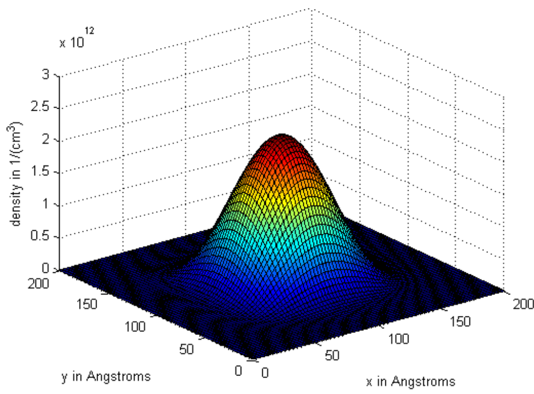

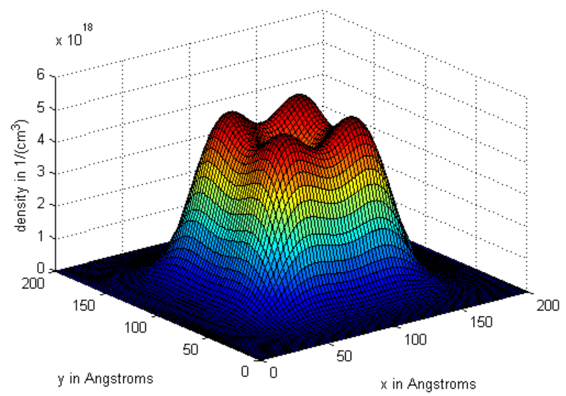

(a) (b)

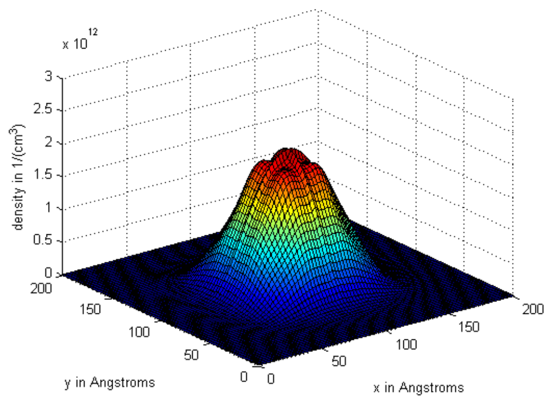

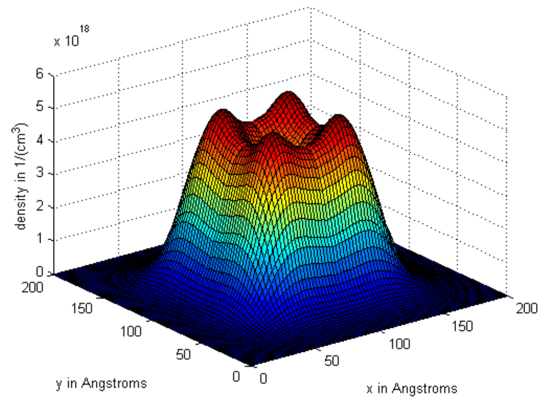

(c) (d)

Figure 3-2: Electron density solutions obtained from the direct method for (a) -0.3V and (b) 0.3V applied to the outer boundary, and density solutions from the CMS approach for (c) -0.3V and (d) 0.3V applied to outer boundary. 60 by 60 mesh domain.

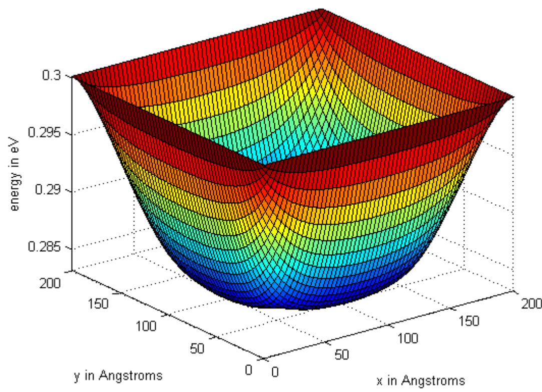

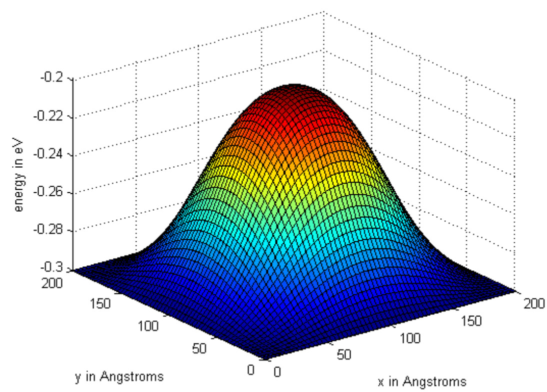

(a) (b)

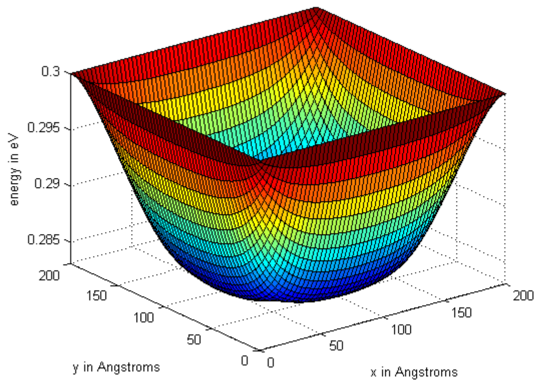

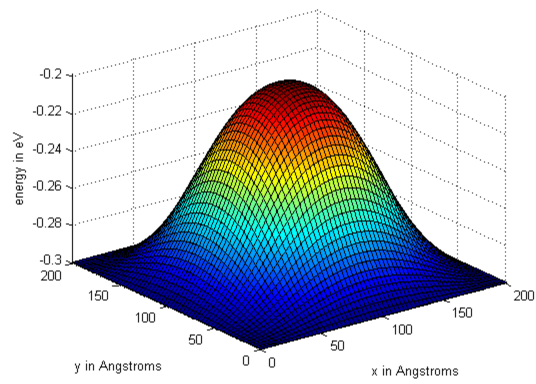

(c) (d)

Figure 3-3: Potential energy solutions ($e\phi$) obtained from the direct method for (a) -0.3V and (b) 0.3V applied to the outer boundary, and potential energy solutions from the CMS approach for (c) -0.3V and (d) 0.3V applied to outer boundary. 60 by 60 mesh domain.

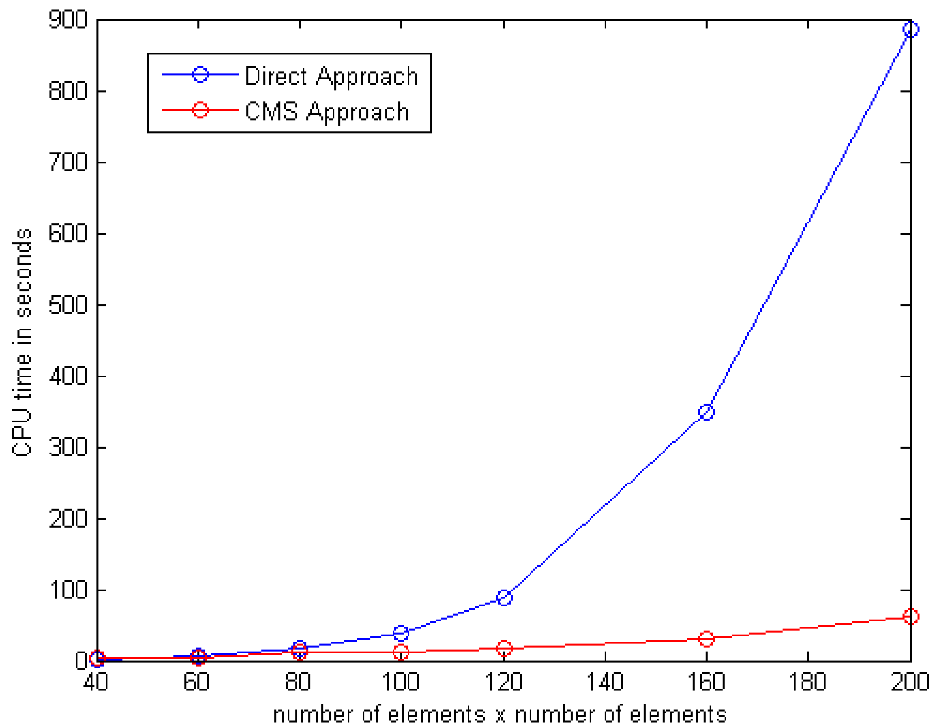

Figure 3-4: A comparison of the CPU time for meshes of different sizes.

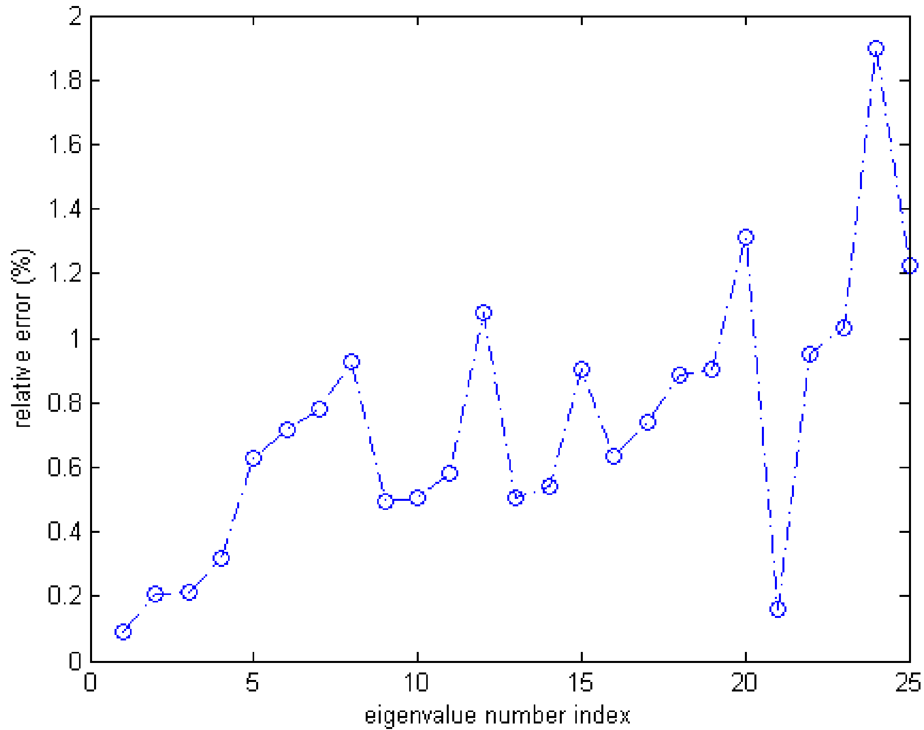

Figure 3-5: Relative error of the eigenvalues obtained from the CMS approach compared with the results obtained from the direct method on a 80 by 80 mesh with Dirichlet boundary conditions.

It is shown in the results that a positive boundary voltage attracts electrons to the boundary. However, electrons moving toward the boundary will be trapped by the potential barrier between GaAs and AlGaAs. When the electrons are repelled by the boundary due to a negative boundary voltage, there is an absence of this "trapping" phenomenon since the electrons can freely move from higher potential energy to lower potential energy but not vice versa. In comparison of the results from the direct and CMS approaches, subtle differences are observed between the two results shown in Figure (3-2). These subtle differences are expected since the number of retained

component eigenvectors is intentionally set to be very small. These differences become smaller when the number of retained modes is increased. The difference is completely eliminated if the number of retained component modes is set to maximum. Figure 3-5 shows the error between the eigenvalue results obtained from the two methods. Figure 3-4 shows the computational cost of the two methods. A significant reduction in computational cost for the CMS approach is observed, especially when the mesh size is large. Figure 3-4 shows that there is no noticeable savings in computation time for the mesh of 40 by 40 elements. However, when the mesh is refined to 200 by 200 elements, the CMS approach is about 15 times faster than the direct approach. The expected savings is expected to go up even further as the mesh size increases beyond 200 by 200 elements.

The CMS approach is tested again on the same quantum well structure, but with a homogeneous Neumann boundary condition for the potential. All the other parameters of the quantum well remain the same. The potential energy and electron density results are shown in Figures 3-6 and 3-7. The results from both methods match quite well. The error comparison of the eigenvalues is shown in Figure 3-8. The behavior of the error is similar to that shown in Figure 3-5 for the Dirichlet boundary case. The CPU performance results are the same for both the Nermann and Dirichlet boundary conditions, since the change in the boundary condition of the Poisson equation does not affect the solution time of the Schrödinger equation. Therefore, the CPU time comparison is not repeated here for the sake of brevity.

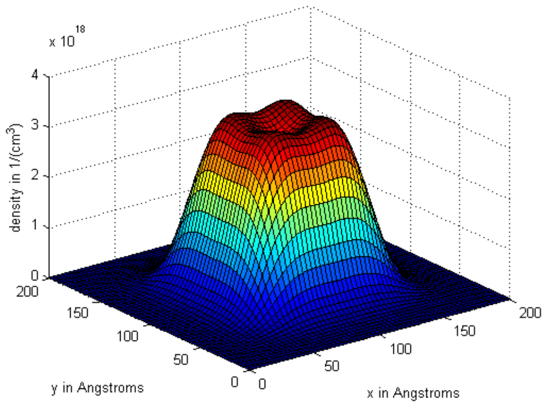

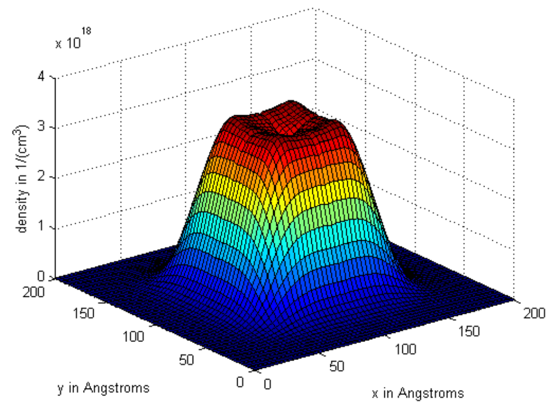

(a) (b)

Figure 3-6: Density solutions for the Neumann boundary case: (a) direct approach and (b) CMS approach. 60 by 60 mesh domain.

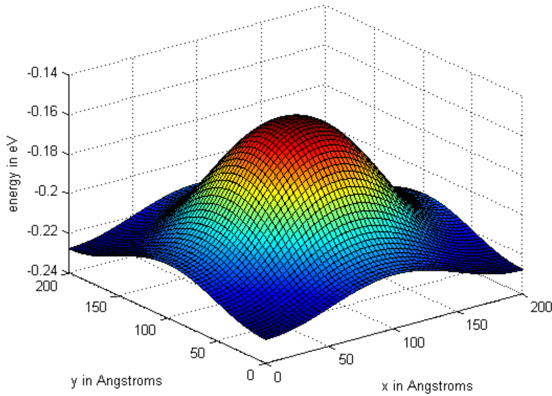

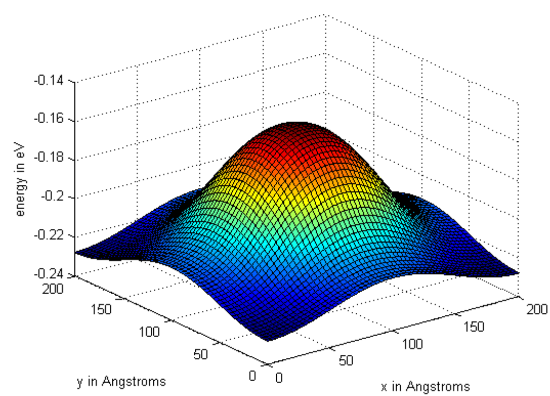

(a) (b)

Figure 3-7: Potential energy solutions for the Neumann boundary case (a) direct approach (b) CMS approach. 60 by 60 mesh domain.

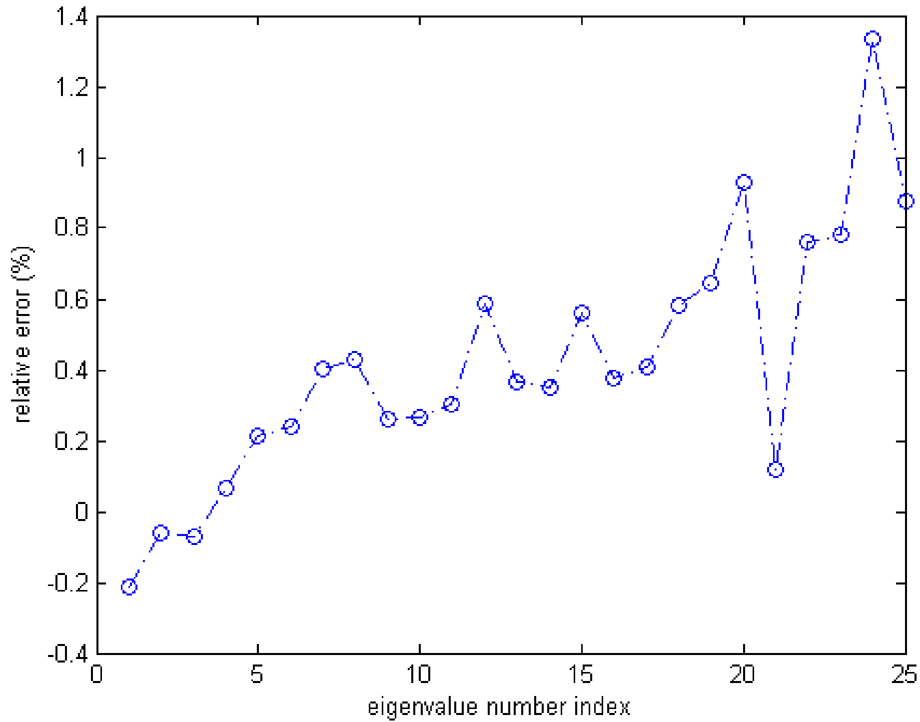

Figure 3-8: Relative error of the eigenvalues obtained from the CMS approach compared with the results obtained from the direct method on a 80 by 80 mesh with Neumann boundary conditions.

The second device simulated in this section is an all-around MOSFET as shown in Figure 3-9. The core of the MOSFET is n-type doped Si with a doping density of 10^{18} $cm^{-3.}$ The dielectric layer surrounding the Si core is SiO_2 with a thickness of 10 Å. In order to obtain a more accurate result of the electron density in the MOSFET, effective mass anisotropicity of Si is accounted for in the simulation by treating the three orthogonal ladders of Si separately. That is, the Schrödinger equation must be solved for each ladder. The electron effective masses are taken to be $0.19m_0$ and $0.91m_0$ for Si in the transverse and longitudinal directions for each ladder, respectively. The electron effective mass for SiO_2 is assumed to isotropic and is set as $0.5m_0$. The heterojunction step potential between Si and SiO_2 is taken to be 3.34 eV. The relative

dielectric constants are set to be 11.9 and 3.9 for Si and SiO_2, respectively. As in the quantum well case, it is found that the lowest 10 eigenpairs are sufficient for an accurate solution. A Dirichlet potential boundary condition of 0.5V was applied to the boundary (gate). For the CMS approach, the domain is further discretized into 4 by 4 components, with 9 component eigenpairs retained in each component. The domain mesh is varied between 40 by 40 elements to 200 by 200 elements for the direct and CMS approaches. Figures 3-10 and 3-11 show the electron density and potential energy profile in the all-around MOSFET for the gate voltage of 0.5V. The results obtained from the direct and CMS approaches are almost identical. The positive gate voltage attracts the electrons in the doped Si towards the SiO2 dielectric layer. The corner effect of the MOSFET is significant. The CPU time comparison is shown in Figure 3-12. It is evident that the computational cost comparison for the all-around MOSFET is very similar to that for the quantum well simulation. When the mesh size is small (small DOFs) the computational cost reduction of the CMS approach is not significant due to the extra matrix calculations associated with the method. The advantage of the CMS approach becomes obvious when the mesh size increases. For this reason, the CMS approach is suitable for simulation of large systems. The relative error of the eigenenergies of the 3 ladders is shown in Figure 3-13. It is shown in the figure that the first and third ladders have the same error. This is due to the fact that the x-y plane is a symmetric plane of the ladders. The error of the second ladder, although different from that of the other two ladders, is in the same order. All results for relative error show a general trend that as the order of eigenvalues increases, the relative error between the direct and CMS results will increase. This is on par with expectations that in general, higher order eigenvalues tend to display more error. However, this error can always be reduced when more component modes are retained in each component.

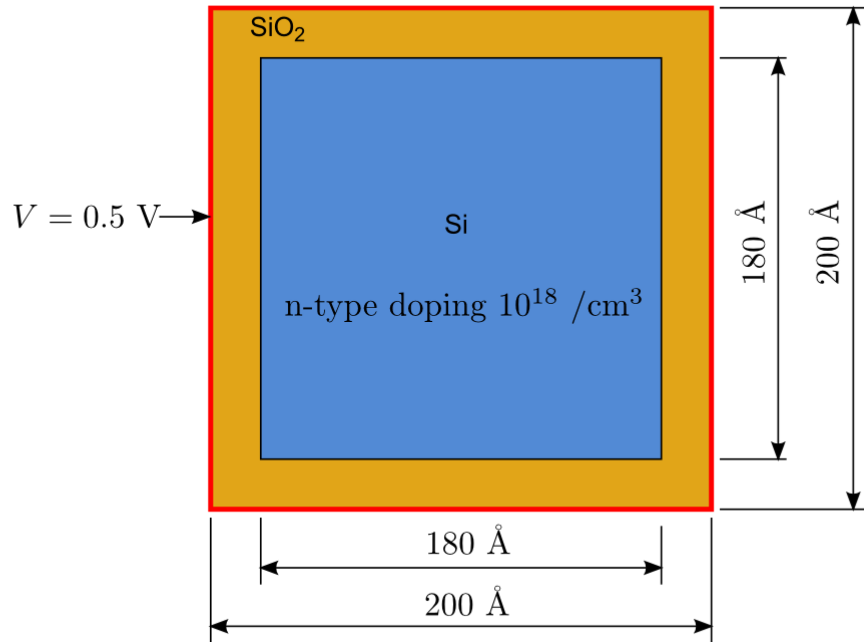

Figure 3-9: Computational domain of an all-around MOSFET.

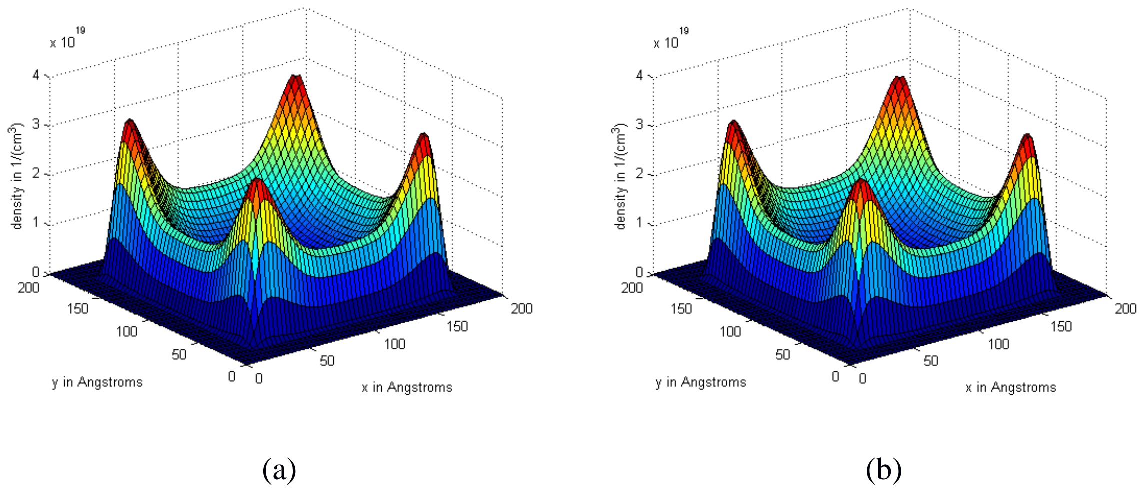

(a) (b)

Figure 3-10: Electron density solutions for the all-around MOSFET: (a) direct approach (b) CMS approach. 60 by 60 mesh domain.

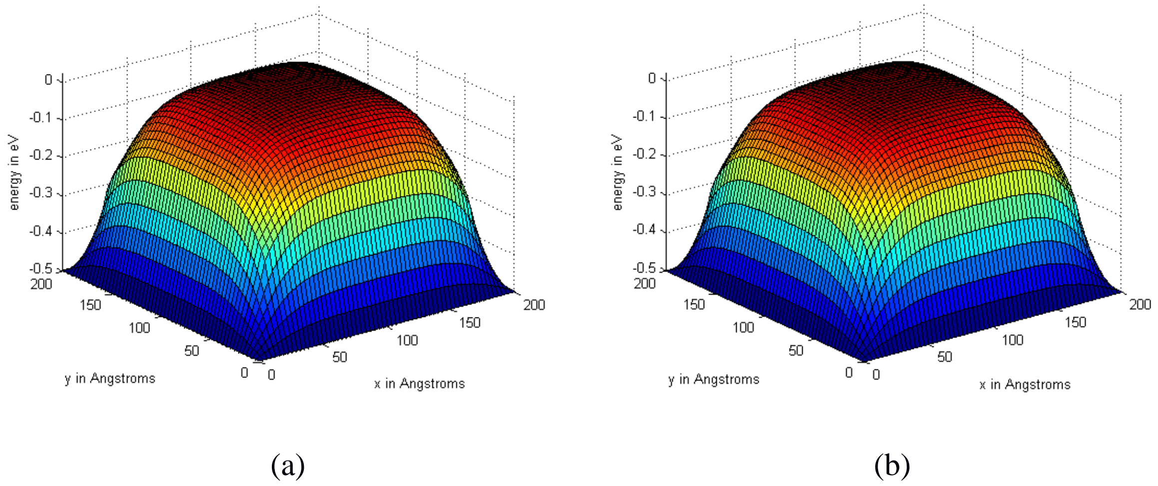

Figure 3-11: Potential energy solutions for the all-around MOSFET: (a) direct approach (b) CMS approach. 60 by 60 mesh domain.

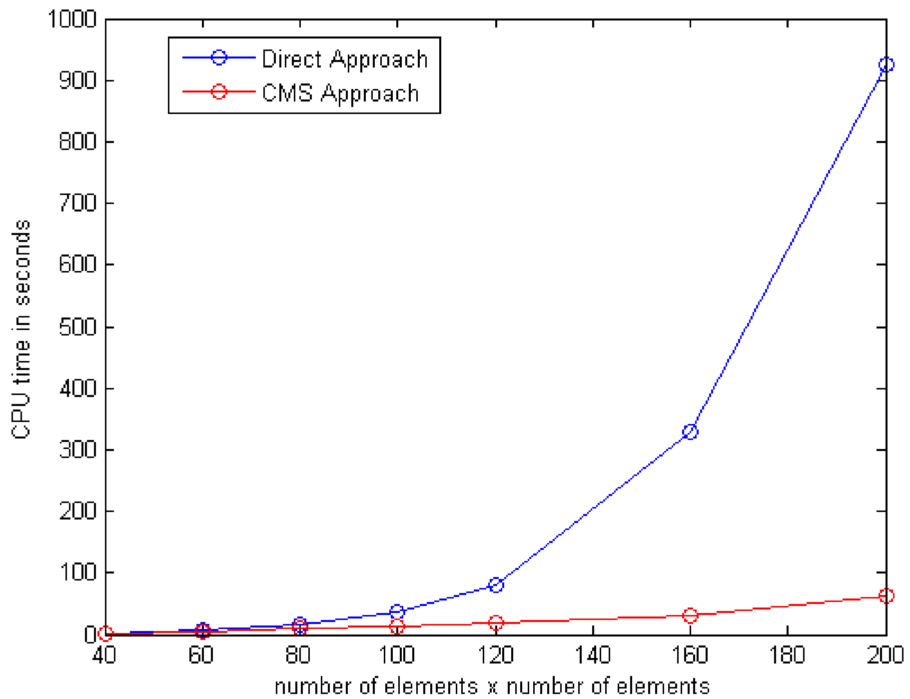

Figure 3-12: Comparison of the CPU times for a single ladder for meshes of different sizes.

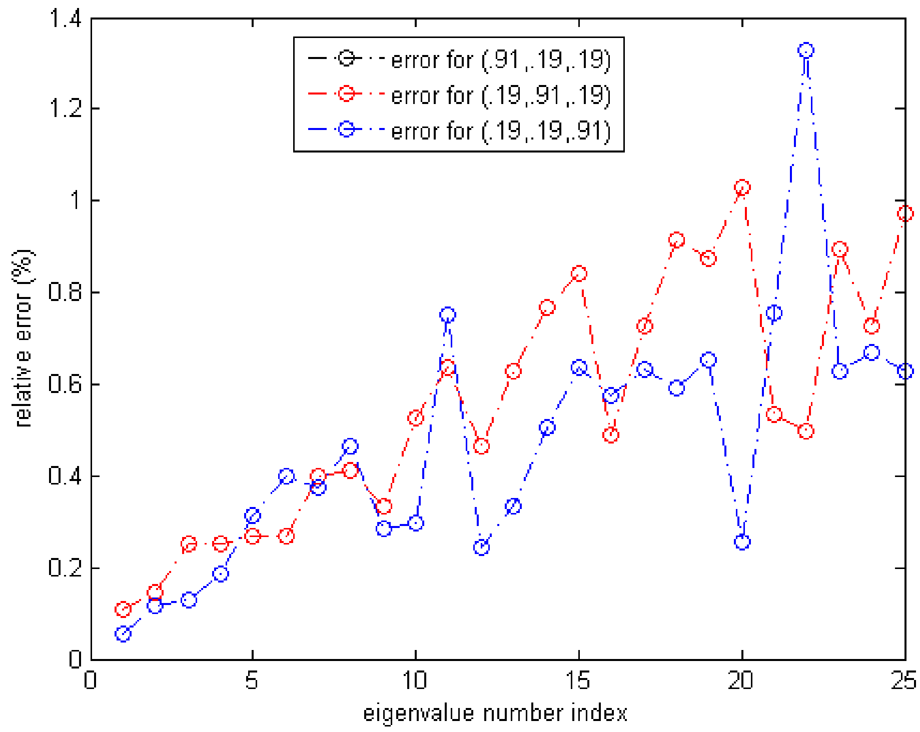

Figure 3-13: Relative error of eigenvalues of the 3 ladders for an 80 by 80 mesh. Legend indicates the relative effective masses in (x,y,z) directions for silicon.

Chapter 4 Quantum Mechanical Electrical Transport Analysis of Nanodevices

Electrostatic analysis is useful to predict the electron distribution responding to varying boundary voltages. However, when there is a current flowing through the device, electrostatic analysis cannot be used to show the current density or the flow of electrons. In such cases, electron transport analysis is necessary. Different from electrostatics, electron transport analysis deals with physical models describing the electrical response of a device when a current passes through. Although the carrier distribution is still governed by the Schrödinger equation and Poisson equations, the wave functions and potential energy at the leads where carriers are injected or drained have to be properly determined. In such cases, states which carry current are more important for the understanding of electron transport through the small device regions. Broadly defined, there are two types of continuum computational approaches for self-consistently solving electron transport problems in nanodevices. The first type is based on the coupled Schrödinger and Poisson equations with open boundary conditions. In this type of approaches, the current-carrying states are considered as a linear combination of the bound states in the device region and the states that extend to infinity along the input and output leads. A representative method in this category is the Quantum Transmitting Boundary Method (QTBM) [27,28]. The second type is nonequilibrium Green's function based approaches [29,30]. In the non-equilibrium Green's function (NEGF) method, instead of coping with the open boundary conditions, a self-energy matrix is introduced. By composing the Hamiltonian for the entire system, the electron density and current density can be obtained through a numerical procedure. In comparison to the NEGF, the QTBM has the advantage of obtaining the full quantum states in

the device. The detailed information of the band valley contributions can be calculated and visualized. However, the method requires solving discretized Schrödinger equation over the device region, which can be time consuming for a large system. In this chapter, we combine the CMS approach with the QTBM to accelerate the numerical solution of the electronic transport problem in nanodevices. We first describe the mathematical formulation of the CMS based QTBM. A numerical example of MOSFET simulation is then presented to demonstrate the performance of the method.

4.1 Quantum Transmitting Boundary Method (QTBM)

QBTM is a method that modifies the implementation of the Schrödinger Poisson equation in order to consider current carrying states. The energy is temporarily discretized by imposing two different boundary conditions at the leads to obtain eigenpairs for the "sine" and "cosine" modes. The standing wave functions obtained from these modes are then decomposed into traveling wave constituents, each of which is used to represent electron injection from an individual lead. In the numerical implementation, as with the Schrödinger-Poisson iteration method, the same mesh can be used for the solution of both Schrödinger and Poisson equations.

In the QTBM, the potential and charge distribution are calculated by seeking a self-consistent solution to the Schrödinger equation with open boundary conditions and the Poisson equation. A 2-D domain illustrating the problem is shown in Figure 4-1. The system consists of a "device region" (shaded region), Ω_0, and a set of leads, Ω_1, Ω_2, Ω_3,…, Ω_n, where n denotes the number of leads. The leads are assumed to have constant width, denoted as d_i. The interface between lead i and Ω_0 is defined as Γ_i. The portion of device region boundary which is not connected to a lead is defined as Γ_0. Note that, as will be discussed in details later, the open

boundary conditions for the current-carrying states are defined on Γ_i, i=1,2,…,n. In order to define the open boundary conditions, a local coordinate system, (ξ_i, η_i), is defined at each lead-device domain interface, as shown in Figure 4-1.

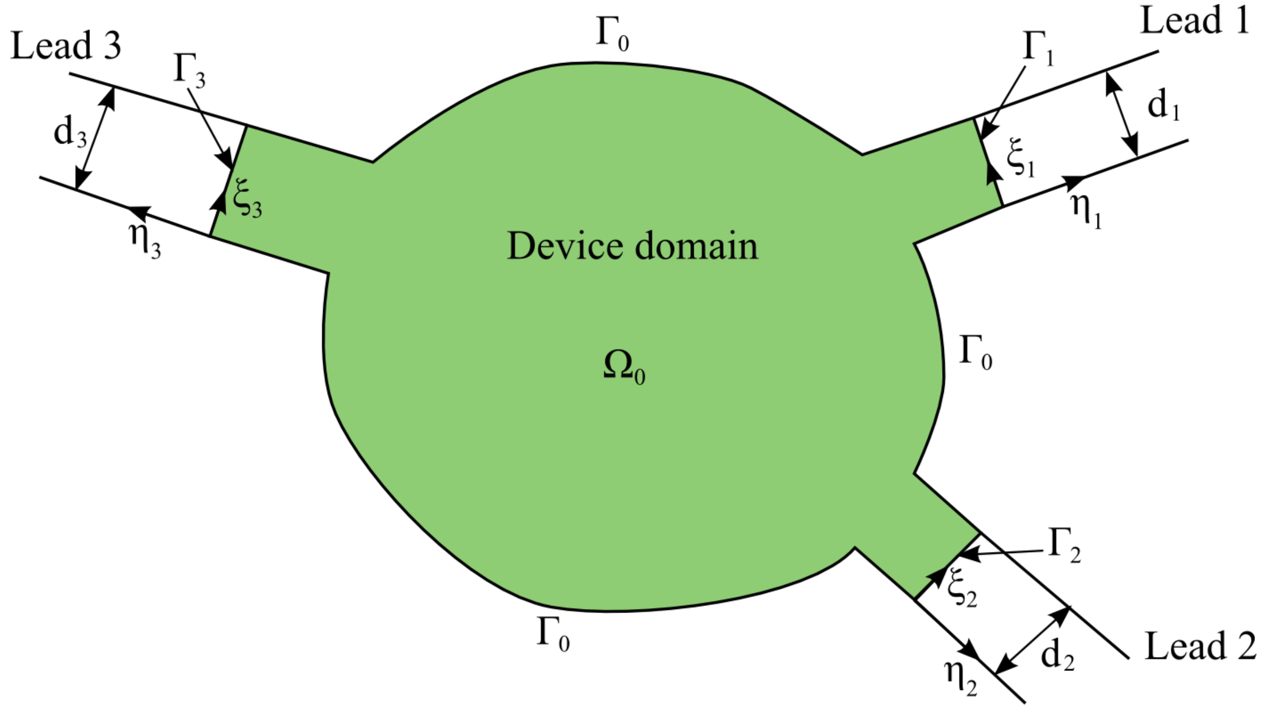

Figure 4-1: 2-D simulation domain for electron transport analysis.

The traveling wave Schrödinger equation to be solved is given by

$$-\frac{\hbar^2}{2m_x^*}\frac{\partial^2\Phi_p}{\partial x^2}-\frac{\hbar^2}{2m_y^*}\frac{\partial^2\Phi_p}{\partial y^2}+U\Phi_p=E_p\Phi_p \tag{4-1}$$

where Φ_p is the traveling wave function corresponding to a given energy E_p. The potential energy and effective masses are the same as those defined in Chapter 2. The 2-D Poisson equation is

also the same as defined in the electrostatic analysis discussed in Chapter 3. For the sake of completeness, it is repeated for a 2-D domain as follows:

$$\epsilon\left(\frac{\partial^2\phi}{\partial x^2}+\frac{\partial^2\phi}{\partial y^2}\right)= -q[-n(\phi)+p(\phi)+ N_D^+ - N_A^-] \tag{4-2}$$

Note that the traveling wave function Φ_p in the Schrödinger equation is obtained for a given energy E_p. A proper sampling scheme of the energy E_p is to use the standing wave solutions with homogeneous Dirichlet or Neumann boundary conditions at the lead-device interfaces [28]. The physical consideration of this scheme is based on the energy resonance condition between the device region and the leads. To obtain the standing wave energies, one needs to solve the bound-state Schrödinger equation in Ω_0 given by

$$-\frac{\hbar^2}{2m_x^*}\frac{\partial^2\Psi_p}{\partial x^2}-\frac{\hbar^2}{2m_y^*}\frac{\partial^2\Psi_p}{\partial y^2}+U\Psi_p = E_p\Psi_p \qquad \text{in } \Omega_0 \tag{4-3}$$

with the boundary conditions

$$\Psi_p\Big|_{\eta_i=0} = 0 \qquad \text{or} \qquad \frac{\partial^2\Psi_p(\eta_i,\xi_i)}{\partial\eta_i}\bigg|_{\eta_i=0} = 0 \qquad \text{on } \Gamma_i \tag{4-4}$$

The first (Dirichlet) and second (Neumann) boundary conditions are referred to as a “sine” or “cosine” boundary conditions. To obtain the standing wave energies, one needs to solve the bound-state Schrödinger equation, Eq. (4-3), in Ω_0 with both “sine” and “cosine” boundary conditions for the three ladders of Silicon. That is, the standing wave Schrödinger equation (Eq. (4-3)) is to be solved 6 times over the 2-D domain of the device. The standing wave solutions obtained can be further denoted as $(\psi_p^{(t,l)}, E_p^{(t,l)})$ where t=s or c and l denotes the ladder associated

with the different conduction band alignments which determine the effective masses m_x^* and m_y^* to be used in the Schrödinger equation. Note that this part of the calculation consumes most of the computational time of the entire simulation. To accelerate the simulation, in this work, we decompose Ω_0 into connecting components and employ the CMS method to construct the standing wave functions and obtain the energies. By using the CMS approach, the computational cost can be largely reduced. As the standing wave Schrödinger equation is solved here, the CMS formulation remains the same as depicted in Chapter 2. The only difference for the current electron transport problem lies in the "cosine" like boundary condition. However, the implementation of the CMS method is straightforward: instead of deleting the rows and columns of the coefficient matrix shown in Eq. (2-16), the DOFs corresponding to the "cosine" boundary nodes are simply retained in the eigen solution of the components. The assembled global wave functions are non-zero at the lead-device interfaces when the "cosine" boundary condition is applied.

Once the standing wave energies, E_p, are calculated by using the CMS approach, the traveling waves at the open boundary (lead-device interface) for the traveling wave Schrödinger equation (Eq. (4-1)) can be written as [28]

$$\Phi_{p,i}(\eta_i,\xi_i) = \sum_{m=1}^{N^i}\left[a_m^i\chi_m^i(\xi_i)e^{-\iota k_m^i\eta_i} + b_m^i\chi_m^i(\xi_i)e^{\iota k_m^i\eta_i}\right] + \sum_{m=N^i+1}^{\infty}\left[a_m^i\chi_m^i(\xi_i)e^{k_m^i\eta_i} + b_m^i\chi_m^i(\xi_i)e^{-k_m^i\eta_i}\right] \tag{4-5}$$

Eq. (4-5) represents the injection condition at the leads. The traveling wave function is expressed as a superposition of a set of plane waves. The exponential functions are the injection and

reflection plane waves ($e^{-\iota k_m^i \eta_i}$ and $e^{\iota k_m^i \eta_i}$, respectively). Note that $\iota = \sqrt{-1}$, which is used to avoid confusion with i which denotes the lead number. Depending on their energy, the plane waves are either injected into the device domain from the leads or reflected back from the device. The amplitudes of the injection and reflection plane waves are determined by the coefficients a_m^i and b_m^i, respectively. The shape of the traveling wave function in the transverse (ξ_i) direction of lead i, χ_m^i, is determined self-consistently by solving 1-D Schrödinger-Poisson equations on Γ_i, i.e.,

$$-\frac{\hbar^2}{2m_{\xi_i}^*}\frac{\partial^2 \chi_m^i}{\partial \xi_i^2} - eV(\xi_i)\chi_m^i = E_m^i \chi_m^i \qquad m = 1,2,\ldots \quad \text{on } \Gamma_i \tag{4-6}$$

$$\epsilon\frac{\partial^2 V}{\partial \xi_i^2} = -q[-n(\xi_i) + p(\xi_i) + N_D^+ - N_A^-] = -\rho(\xi_i) \qquad \text{on } \Gamma_i \tag{4-7}$$

The boundary conditions of the 1-D Schrödinger equation is given by

$$\chi_m^i(0) = \chi_m^i(d_i) = 0 \tag{4-8}$$

and the normalization condition being

$$\int_o^{d_i} \chi_l^i(\xi_i)\, \chi_m^i(\xi_i) d\xi_i = \delta_{l,m} \tag{4-9}$$

where l and m are eigenstates of the system and δ is the Dirac delta function defined by:

$$\delta_{l,m} = \begin{cases} 1 & if\ l = m \\ 0 & if\ l \neq m \end{cases} \tag{4-10}$$

By solving the 1-D Schrödinger equation, the eigenpairs $\{\chi_m^i(\xi_i), E_m^i,\}$ can be obtained. The eigenpairs can then be used to calculate the charge density along Γ_i. The charge density along the 1-D domain is given by

$$n(\xi_i) = \sum_l \sum_m \frac{g_v^{(l)} k_B T \sqrt{m_{\eta_i}^{*(l)} m_z^{*(l)}}}{\pi \hbar^2} ln\left[1 + exp\left(\frac{E_F^i - E_m^{i,l}}{k_B T}\right)\right] \left|\chi_m^{i,l}(\xi_i)\right|^2 \qquad (4\text{-}11)$$

where E_F^i is the quasi-Fermi level at lead i. The charge density obtained is then substituted into the right hand side of the 1-D Poisson equation. The boundary condition of the 1-D Poisson equation is given by

$$\left.\frac{\partial V}{\partial \xi_i}\right|_{\xi_i=0} = \left.\frac{\partial V}{\partial \xi_i}\right|_{\xi_i=d_i} = 0 \qquad (4\text{-}12)$$

The Neumann boundary condition given in Eq. (4-12) does not ensure a unique solution of the Poisson equation. A unique solution of the potential can be obtained by enforcing the charge neutrality condition in the 1-D domain, i.e.,

$$\int_0^{d_i} \rho(\xi_i) d\xi_i = 0 \qquad (4\text{-}13)$$

In the numerical implementation, the charge neutrality condition is enforced by adjusting the Fermi level using the bi-section method [38]. The charge density distribution which satisfies the charge neutrality condition is then used to calculate the right hand side of the Poisson equation. A Dirichlet condition V=0 is applied at the midpoint of the interface Γ_i when the Poisson equation is solved. The new potential solution obtained from the Poisson equation is applied in the Schrödinger equation to compute the new eigenenergies and wave functions. The iteration

continues until self-consistent solutions of the potential, eigenpairs, Fermi level and charge density are obtained. In typical simulation of electronic devices, Fermi levels are prescribed at the leads. Therefore, in our simulations, the Fermi levels obtained from the 1-D Schrödinger-Poisson equations are shifted to the prescribed values. Accordingly, the eigenenergy and potential solutions in the leads are also shifted by the same amount. Subsequently, the wave vector $\mathrm{k_m^i}$ in Eq. (4-5) can be calculated as follows:

$$k_m^i = \begin{cases} \sqrt{\dfrac{2\mathrm{m_{\eta_i}}\left(\mathrm{E_p} - \mathrm{E_m^i}\right)}{\hbar^2}} & \text{for} \quad \mathrm{E_p} \geq \mathrm{E_m^i} \\ \sqrt{\dfrac{2\mathrm{m_{\eta_i}}\left(\mathrm{E_m^i} - \mathrm{E_p}\right)}{\hbar^2}} & \text{for} \quad \mathrm{E_p} < \mathrm{E_m^i} \end{cases} \tag{4-14}$$

where $\mathrm{E_p}$ and $\mathrm{E_m^i}$ are the 2-D and 1-D standing wave energies in the device domain and on the lead-device interface. In Eq. (4-5), N^i is the number of traveling waves in lead i, or put differently, the maximum m such that $E_m^i \leq E_p$. It can be shown that the injection magnitude can be written as

$$a_m^i = \frac{1}{2}\int_o^{d_i} \chi_m^i(\xi_i)\,\Psi_p(\eta_i = 0, \xi_i)\,d\xi_i \tag{4-15}$$

for the “cosine” mode and

$$a_m^i = \begin{cases} \iota\dfrac{1}{2k_m^i}\displaystyle\int_0^{d_i} \chi_m^i(\xi_i)\dfrac{\partial\psi_p(\eta_i = 0, \xi_i)}{\partial\eta}d\xi_i, & 1 \leq m \leq N^i \\ \dfrac{1}{2k_m^i}\displaystyle\int_0^{d_i} \chi_m^i(\xi_i)\dfrac{\partial\psi_p(\eta_i = 0, \xi_i)}{\partial\eta}d\xi_i, & m \geq N^i \end{cases} \tag{4-16}$$

for the “sine” mode. The reflection magnitude can be obtained by using the orthogonal condition of the 1-D wave functions

$$\int_{o}^{d_i} \chi_m^i(\xi_i)\, \Phi_{p,i}(\eta_i = 0, \xi_i) d\xi_i = a_m^i + b_m^i \qquad (4\text{-}17)$$

i.e.,

$$b_m^i = \int_{o}^{d_i} \chi_m^i(\xi_i)\, \Phi_{p,i}(\eta_i = 0, \xi_i) d\xi_i - a_m^i \qquad (4\text{-}18)$$

The partial derivative of $\Phi_{p,i}(\eta_i, \xi_i)$ with respect to η_i, evaluated at $\eta_i=0$ is

$$\left.\frac{\partial \Phi_{p,i}(\eta_i, \xi_i)}{\partial \eta_i}\right|_{\eta_i=0} = \sum_{m=1}^{N^i} \left[-\iota k_m^i a_m^i \chi_m^i(\xi_i) + \iota k_m^i b_m^i \chi_m^i(\xi_i)\right] + \sum_{m=N^i+1}^{\infty} \left[k_m^i a_m^i \chi_m^i(\xi_i) - k_m^i b_m^i \chi_m^i(\xi_i)\right] \qquad (4\text{-}19)$$

Substituting the expression of a_m^i and b_m^i into Eq. (4-19), one obtains

$$\nabla \Phi_{p,i} \cdot \hat{n}_{\Gamma_i} = \sum_{m=1}^{N} -2\iota k_m^i a_m^i \chi_m^i(\xi_i) + \iota k_m^i \chi_m^i(\xi_i) \int_{o}^{d_i} \chi_m^i(\xi_i)\, \Phi_{p,i}(\eta_i = 0, \xi_i) d\xi_i + \sum_{m=N+1}^{\infty} 2\iota k_m^i a_m^i \chi_m^i(\xi_i) - \iota k_m^i \chi_m^i(\xi_i) \int_{o}^{d_i} \chi_m^i(\xi_i)\, \Phi_{p,i}(\eta_i = 0, \xi_i) d\xi_i \qquad (4\text{-}20)$$

Eq. (4-20) is the Neumann boundary condition for the open leads of the device. Combining the open boundary condition with the traveling wave Schrödinger equation given in Eq. (4-3), for a given energy Ep, the traveling wave function can be obtained. By following the standard finite element discretization scheme, a linear system of equations can be obtained from Eq. (4-3) as

$$\left(\mathbf{T} + \mathbf{V} + \sum_i \mathbf{C}_i - E_p \mathbf{M}\right) \mathbf{\Phi}_{p,i} = \mathbf{P}_i \qquad i = 1,2,\ldots,n \tag{4-21}$$

where

$$\mathbf{P}_i = \frac{-\hbar^2}{2}\left(\sum_{m=1}^{N^i} \frac{1}{m^*_{\eta_i}} 2\imath k^i_m a^i_m \boldsymbol{N}^{\boldsymbol{T}}_{\boldsymbol{i,m}} - \sum_{m=N^i+1}^{\infty} \frac{1}{m^*_{\eta_i}} 2k^i_m a^i_m \boldsymbol{N}^{\boldsymbol{T}}_{\boldsymbol{i,m}}\right) \tag{4-22}$$

$$\boldsymbol{C}_i = \frac{-\hbar^2}{2}\left(\sum_{m=1}^{N^i} \frac{1}{m_{\eta_i}} \imath k^i_m \boldsymbol{N}^{\boldsymbol{T}}_{\boldsymbol{i,m}} \boldsymbol{N}_{\boldsymbol{i,m}} - \sum_{m=N^i+1}^{\infty} \frac{1}{m_{\eta_i}} k^i_m \boldsymbol{N}^{\boldsymbol{T}}_{\boldsymbol{i,m}} \boldsymbol{N}_{\boldsymbol{i,m}}\right) \tag{4-23}$$

And

$$\boldsymbol{N}_{\boldsymbol{i,m}} = \int_0^{d_i} \chi^i_m(\xi_i) \begin{bmatrix} N_1 \\ N_2 \end{bmatrix} d\xi_i \tag{4-24}$$

where N_1 and N_2 are the 1-D finite element shape functions defined on the line elements on Γ_i. Note that the open boundary condition shown in Eq. (4-20) is applied at the leads with the waves injected from one lead at a time. When the wave is injected from lead i, both $\mathbf{P}_i$ and $\mathbf{C}_i$ are nonzero. For all other leads $j \neq i$, $a^i_m = 0$ with b^i_m to be determined from Eq. (4-18). Therefore, $\mathbf{P}_j$=0 for $j \neq i$ and $\mathbf{C}_j$ is still computed from Eq. (4-23).

Once $\Phi_{p,i}$ is obtained by solving the linear system given by Eq. (4-21), the decomposition of traveling wave functions must be summed to ensure that the summation of these decomposed wave functions match the result obtained from the standing wave analysis. In other words, a check must be done in the following fashion:

$$\sum_{i=1}^{n} \Phi_{p,i} = \psi_p \tag{4-25}$$

However, in most cases, this check fails. In the event of a failure to obtain the desired result mentioned in the above equation, the traveling wave functions are scaled to satisfy Eq. (4-25). The scaling scheme is established to seek constants a_i to be multiplied to $\Phi_{p,i}$ in order to satisfy the following condition [28]:

$$\sum_{j=1}^{n} \int_{\Omega_0} (\Phi_{p,i}^{*} \Phi_{p,j} dr)\, a_j = \int_{\Omega_0} (\Phi_{p,i}^{*} \psi_p dr) \tag{4-26}$$

Eq. (4-26) results in a nxn linear system whose coefficient matrix is often singular. To obtain the solution of a_i , pseudo-inverse of the coefficient matrix is computed by using the singular value decomposition method. The pseudo-inverse of the coefficient matrix is then multiplied to the right-hand side vector to obtain the unknown a_i. After a_i's are obtained, $\Phi_{p,i}$ is then replaced with $a_i \Phi_{p,i}$. Once $\Phi_{p,i}$ (updated to in actuality to be $a_i \Phi_{p,i}$) is found, in order to compute the charge density, it must be renormalized as

$$\int_{\Omega_0} \left(\sum_{i=1}^{n} \left| \Phi_{p,i}^{(t,l)} \right|^2 \right) dr = \frac{1}{2} \qquad t = s\ or\ c \tag{4-27}$$

The factor ½ is due to the fact that the "sine" and "cosine" modes are summed in the calculation of the charge density. Each mode accounts for half of the occupancy probability.

After the traveling wave functions are calculated, the charge density within the device domain can be computed as

$$n(r) = \sum_{l} \sum_{t=s,c} \sum_{p=1}^{\infty} \sum_{i=1}^{n} \left\{ \sum_{m=1}^{\infty} c_m^i(p,t,l) \rho[k_m^i(p,t,l), k_D^i, E_p^{(t,l)}, T] \right\} \left| \Phi_{p,i}^{(t,l)}(r) \right|^2 \tag{4-28}$$

where $c_m^i(p,t,l)$ is the amplitude normalization factor given by

$$c_m^i(p,t,l) = \frac{\left| a_m^i(p,t,l) \right|^2}{\sum_{m=1}^{\infty} \left| a_m^i(p,t,l) \right|^2} \tag{4-29}$$

and

$$\rho[k_m^i(p,t,l), k_D^i, E_p^{(t,l)}, T] = \left(g_v^{(l)} \sqrt{\frac{2m_z^{*(l)} k_B T}{\pi \hbar^2}} \right) F_{-1/2} \left(\frac{E_F^i - E_p - \left(\hbar^2 / 2m_{\eta_i}^{*(l)} \right) k_D^i (k_D^i - k_m^i(p,t,l))}{k_B T} \right) \tag{4-30}$$

Where $F_{-1/2}$ is the complete Fermi-Dirac integral of order -1/2, E_F^i is the Fermi-level at the leads, and k_D^i is the drift wave vector determined by the current continuity condition. The current continuity condition at the lead-device interfaces is simply

$$J_{dev}^i = J_{lead}^i \tag{4-31}$$

Eq. (4-31) can be expanded as

$$e\int_0^{d_i}\left\{\sum_{i,p,t,l}\left(\frac{-\iota\hbar}{2m_{\eta_i}^{*(l)}}\right)\left[\sum_{m=1}^{\infty}c_m^i(p,t,l)\rho[k_m^i(p,t,l),k_D^i,E_p^{(t,l)},T]\right]\left[\left(\frac{\partial\Phi_{\mathrm{p,i}}^{(\mathrm{t,l})}}{\partial(-\hat{\mathrm{n}})}\right)^*\Phi_{\mathrm{p,i}}^{(\mathrm{t,l})}\right.\right.$$
$$\left.\left.-\frac{\partial\Phi_{\mathrm{p,i}}^{(\mathrm{t,l})}}{\partial(-\hat{\mathrm{n}})}\left(\Phi_{\mathrm{p,i}}^{(\mathrm{t,l})}\right)^*\right]\right\}d\xi_i=-e\frac{\hbar k_D^i}{2m_{cond}^i}\int_0^{d_i}N_D(\xi_i)\,d\xi_i \tag{4-32}$$

where a positive k_D^i implies additional electron injection into the device domain, m_{cond}^i is the conductivity effective mass of the lead i with $\frac{1}{m_{cond}^i}=[\sum_l\left(g_v^{(l)}/m_{\eta_i}^{*(l)}\right)]/\sum_l g_v^{(l)}$, and $N_D(\xi_i)$ is the donor concentration which is taken to approximate the electron density along the lead. In our simulations, we observed that k_D^i is quite small except for high gate voltages. Therefore, it is reasonable to neglect k_D^i for moderate gate voltages.

After the charge density is calculated from Eq. (4-28), the right hand-side of the Poisson equation (Eq. (4-2)) can be evaluated. The Poisson equation is then solved over the 2-D device domain. The potential energy in the 2-D standing wave and traveling wave Schrödinger equations are updated by using the potential solution of the Poisson equation. The iteration described above represents the global iteration between the Schrödinger and Poisson equations. Due to the strong nonlinear dependence of the potential, wave functions and the charge density, it often fails to reach convergence of the global iteration through simple relaxation. Numerical techniques such as Newton-Raphson method and under-relaxation method, or re-formulation of the Poisson equation have been employed to ensure or accelerate the convergence as discussed in Chapter 3. In this chapter, for the sake of simplicity of the implementation, we employ the under-relaxation method. The potential in the device domain is updated by

$$\phi_{new}^{k} = \beta\phi^{k} + (1-\beta)\phi^{k-1} \quad (4\text{-}33)$$

Where ϕ^{k-1} is the potential obtained from the previous iteration, ϕ^{k} is the potential obtained from the Poisson equation in the current iteration, ϕ_{new}^{k} is the updated potential which will be applied in the Schrödinger equations in the next iteration and β is the under-relaxation factor. We note that $\beta \leq 0.2$ is a good choice for the MOSFET simulations shown in the next section.

4.1 Numerical Results

In this section, a double-gate MOSFET is simulated by using the CMS based QTBM described in the previous section. As shown in Figure 4-2 (a), the double-gate MOSFET is composed of a Si center channel sandwiched by two SiO_2 layers. Two gate leads are attached to the top and bottom of the SiO_2 layers. The total length of the device is 200 Å. The thickness of the SiO_2 layers is 10 Å. The thickness of the center channel is 30 Å. The center part of the channel is intrinsic Si. The left and right regions are the source and drain, respectively. Both the source and drain are heavily doped with a doping density of $10^{20}/cm^3$. Left and right leads are attached to the source and drain, respectively. Figure 4-2 (b) shows the simulation domain in which the Schrödinger equations are solved. Material properties and boundary conditions are shown in the figure. Note that both the standing wave and traveling wave Schrödinger equations are solved over the same domain Ω_0. Homogeneous Dirichlet boundary condition is applied on the boundary portion occupied by the SiO_2 layer. The boundary conditions on the leads connected to the source and drain are shown in the figure for the two set of simulation conditions (standing wave and traveling wave). Figure 4-2 (c) shows the simulation domain, material properties and boundary conditions for the Poisson equation.

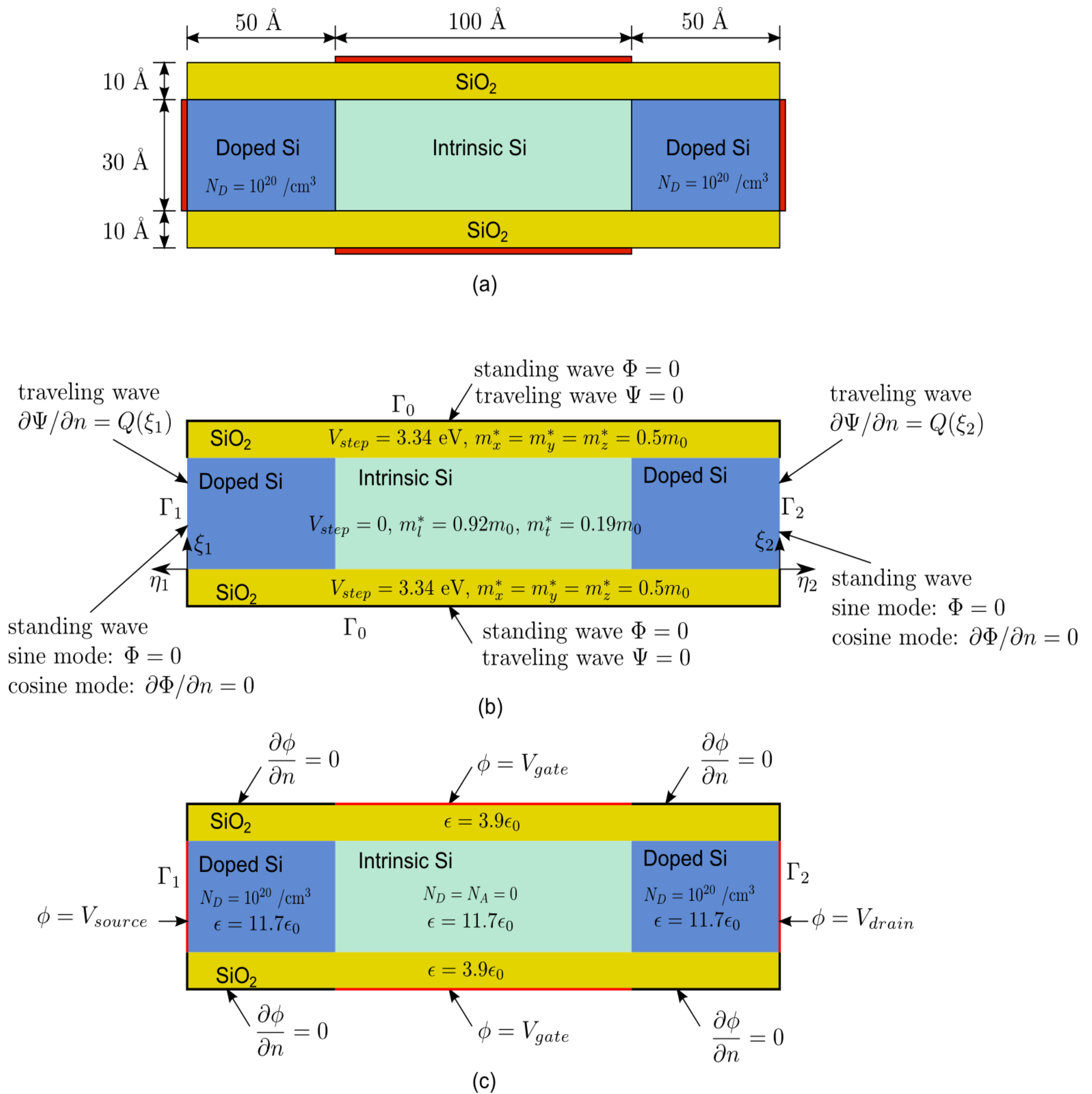

Figure 4-2: Double-gate MOSFET and its simulation domains.

Figures 4-3 ~ 4-8 show the QTBM and CMS based QTBM solutions of the potential energy profiles and electron density distributions in the double-gate MOSFET for the gate voltage of 0V, 0.2V and 0.4V. The results obtained from the direct and CMS approaches are almost identical. Effect of gate voltage on the potential energy and electron density in the MOSFET channel is clearly depicted by the results. The CPU time comparison for simulation cases when 10 and 40 (global) eigenenergies are employed for the electron density calculation is shown in Figures 4-9 and 4-10. Once again, when the mesh size is small the computational cost reduction of the CMS approach is not significant while the CMS approach is 4 times faster for a mesh with more than 25,000 elements. It is evident that the CMS based QTBM solver is advantageous for solving large electron transport problems.

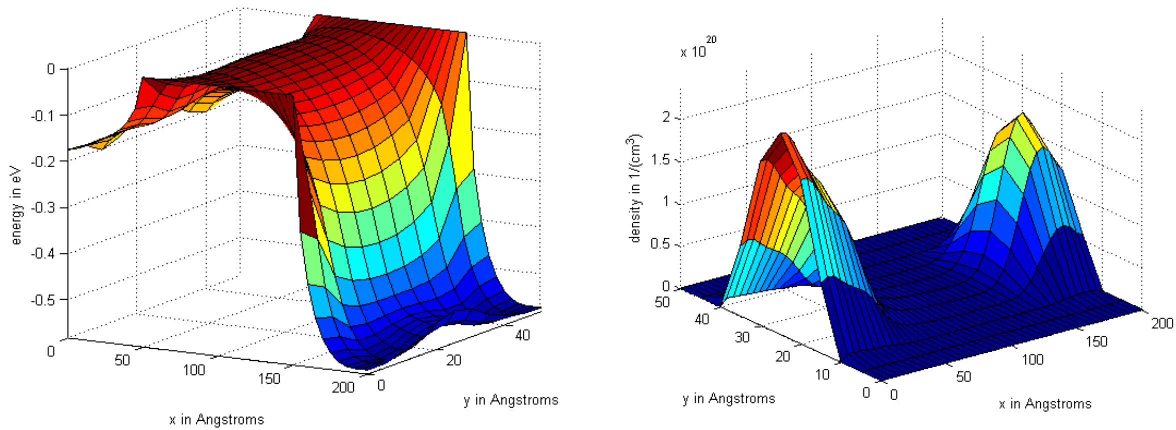

Figure 4-3: Numerical solutions obtained from QTBM for Vg=0V. Left: potential energy. Right: electron density. 40 by 10 mesh domain.

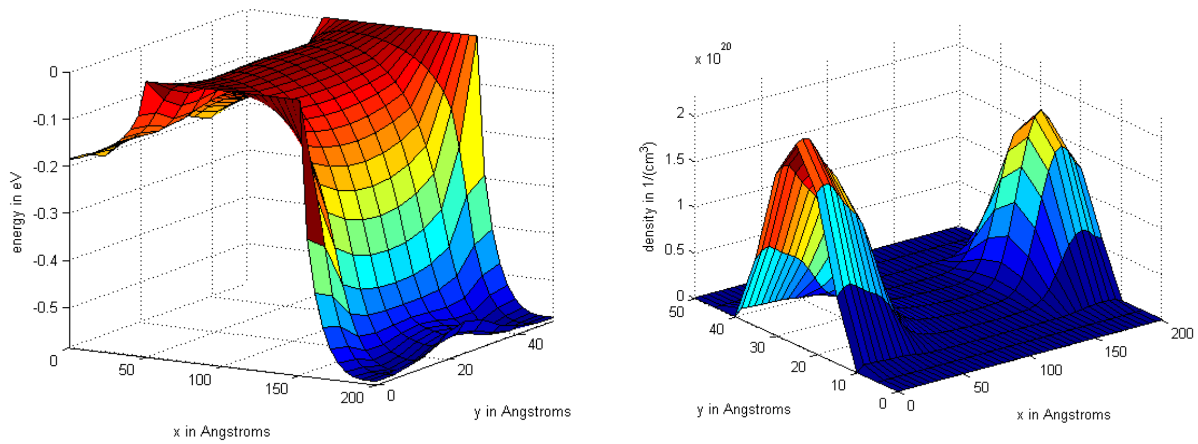

Figure 4-4: Numerical solutions obtained from CMS based QTBM for Vg=0V. Left: potential energy. Right: electron density. 40 by 10 mesh domain.

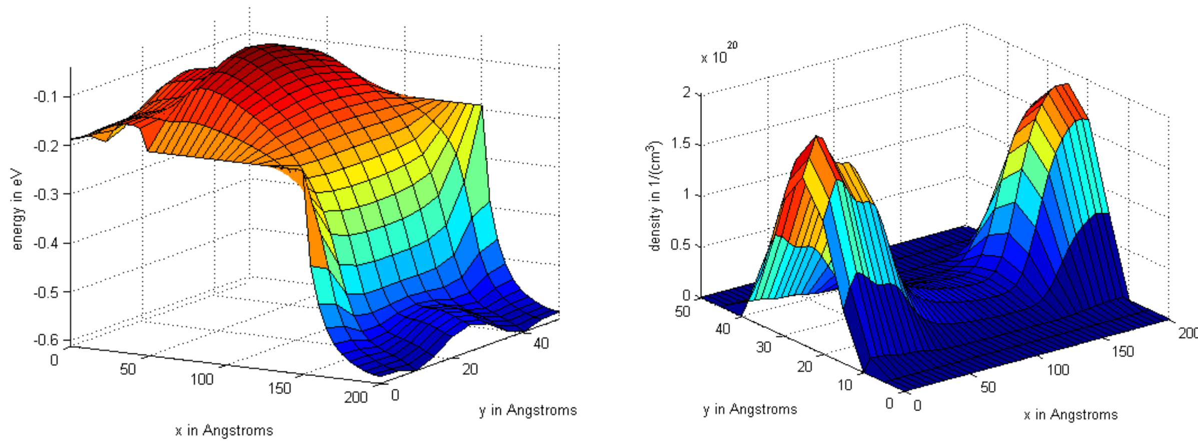

Figure 4-5: Numerical solutions obtained from QTBM for Vg=0.2V. Left: potential energy. Right: electron density. 40 by 10 mesh domain.

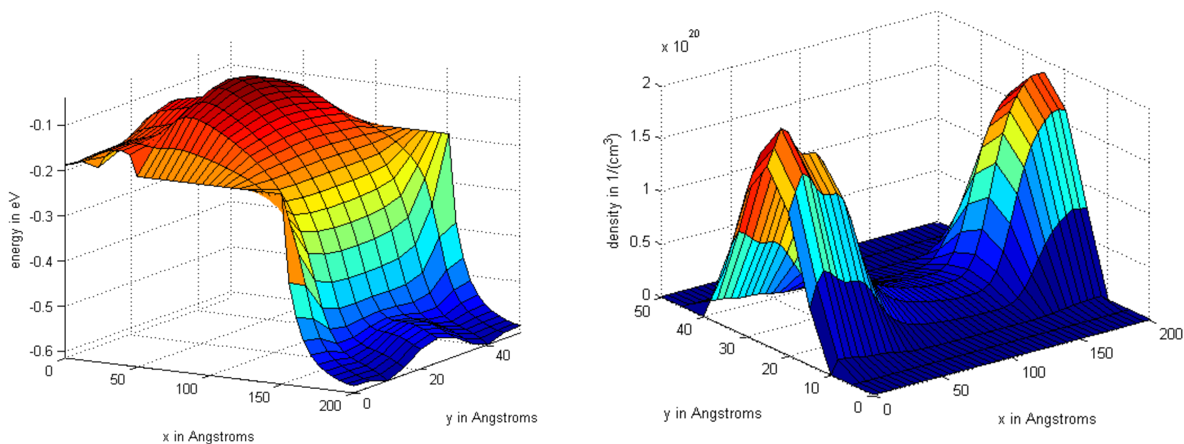

Figure 4-6: Numerical solutions obtained from CMS based QTBM for Vg=0.2V. Left: potential energy. Right: electron density. 40 by 10 mesh domain.

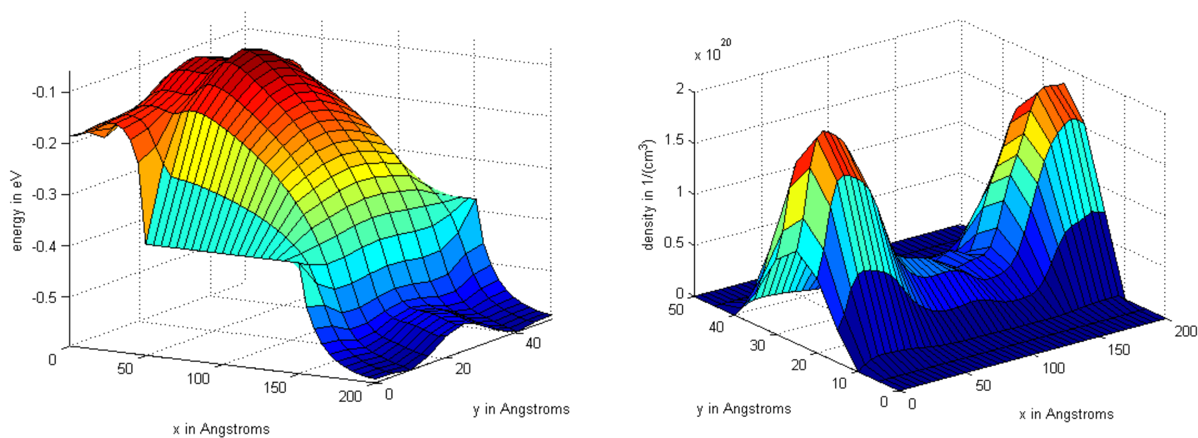

Figure 4-7: Numerical solutions obtained from QTBM for Vg=0.4V. Left: potential energy. Right: electron density. 40 by 10 mesh domain.

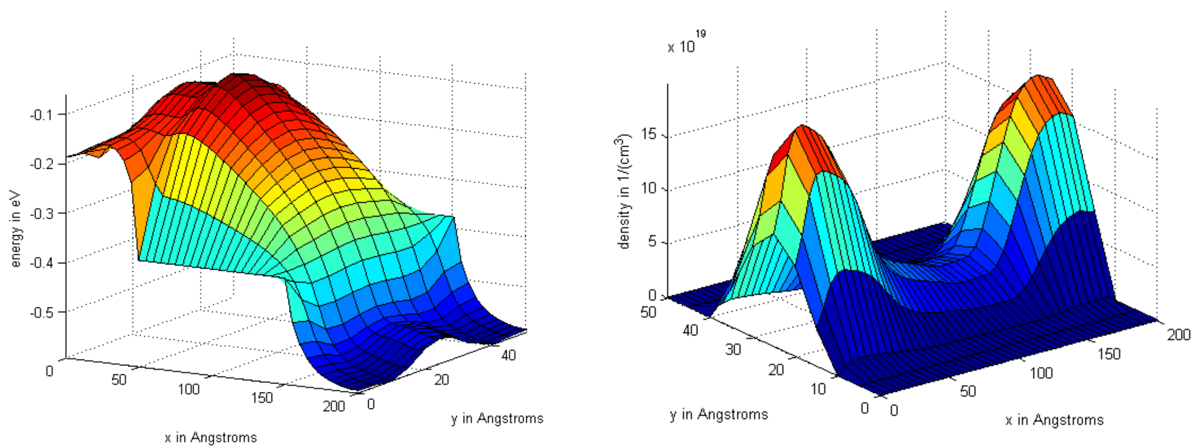

Figure 4-8: Numerical solutions obtained from CMS based QTBM for Vg=0.4V. Left: potential energy. Right: electron density. 40 by 10 mesh domain.

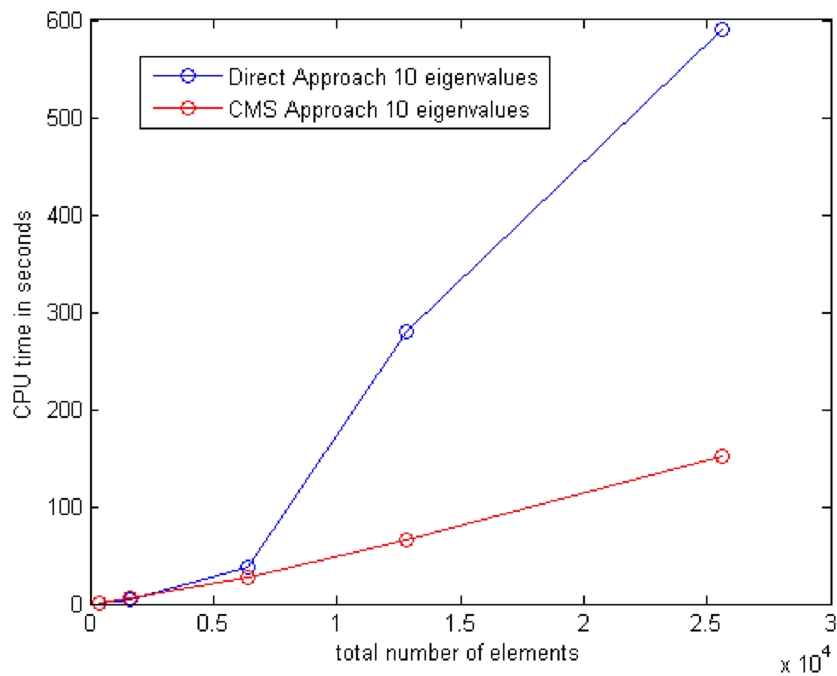

Figure 4-9: Comparison of the CPU times for meshes of different sizes: 10 retained eigenvalues.

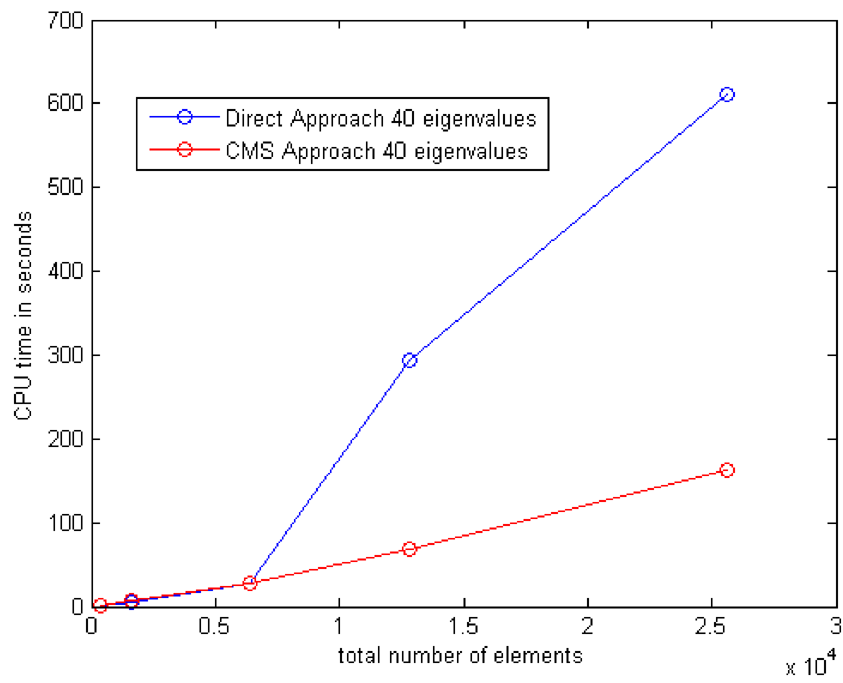

Figure 4-10: Comparison of the CPU times for meshes of different sizes: 40 retained eigenvalues.

Chapter 5 Conclusions and Future Work

In this work, a component mode synthesis (CMS) approach is presented for 2-D quantum mechanical electrostatic and electron transport analysis of nanoscale structures and devices with arbitrary geometries. In the CMS approach, a nanostructure is divided into a set of substructures or components and the eigenvalues (energy levels) and eigenvectors (wave functions) are computed first for all the substructures. The computed wave functions are then combined with constraint or attachment modes to construct a transformation matrix. By using the transformation matrix, a reduced-order system of the Schrödinger equation is obtained for the entire nanostructure. The global energy levels and wave functions can be obtained with the reduced-order system. Through an iteration procedure between the Schrödinger and Poisson equations, a self-consistent solution for charge concentration and potential profile can be obtained. In this work, the CMS approach is established and formulated within the general Schrödinger-Poisson framework for both electrostatic and electron transport scenarios. The CMS approaches are employed to compute the charge concentrations and potential profiles of several nanoscale structures and devices, including an electrostatic quantum wire, an electrostatic all-around MOSFET and a current-transport double-gate MOSFET. The results obtained from the CMS approaches are compared with those obtained from the direct approaches. It is shown that the CMS approach can yield accurate results with much less computational cost compared to the direct finite element analysis. The reduction of computational cost becomes more significant as the total degrees of freedom of the system increase.

We have noticed that there is an optimal combination of the number of components and the number of retained component eigenpairs. Future work could be done to investigate this optimal combination to balance accuracy and efficiency. In addition, only the fixed interface CMS method was implemented. Free interface CMS method is worth investigating to see the advantages and disadvantages of such a method.

References

1. D. Scansen. “Intel putting on fins at 22 nm”, *EE Times*, 1602, 14 (2011).

2. T. Skotnicki, J. A. Hutchby, T. King, H-S. P. Wong and F. Boeuf. “The end of CMOS scaling: toward the introduction of new materials and structural changes to improve MOSFET performance”, *IEEE Circuits and Devices Magazine*, 21(1), 16-26 (2005).

3. Z. Tang, Y. Xu, G. Li and N. R. Aluru, ``Physical Models for Coupled Electromechanical Analysis of Silicon Nanoelectromechanical Systems", *Journal of Applied Physics*, 97(11), 114304 (2005).

4. W. W. Jang, J-B. Yoon, M-S. Kim, J-M. Lee, S-M. Kim, E-J. Yoon, K. H. Cho, S-Y. Lee, I-H. Choi, D-W. Kim and D. Park. “NEMS switch with 30 nm-thick beam and 20 nm-thick air-gap for high density non-volatile memory applications”, *Solid State Electronics*, 52(10), 1578–1583, 2008.

5. X. L. Feng, R. He, P. Yang and M. L. Roukes, “very high frequency silicon nanowire electromechanical resonators”, *Nano Letters*, 7(7), 1953-1959 (2007).

6. Y. Xia, P. Yang, Y. Sun, Y. Wu, B. Mayers, B. Gates, Y. Yin, F. Kim, and H. Yan. “One-dimensional nanostructures: Synthesis, characterization, and applications”, *Advanced Materials*, 15(5), 353–389 (2003).

7. A. S. Arico, P. Bruce, B. Scrosati, J.-M. Tarascon, and W. V. Schalkwijk. “Nanostructured materials for advanced energy conversion and storage devices”, *Nature Materials*, 4, 366–377 (2005).

8. P. T. Hammond. “Form and function in multilayer assembly: New applications at the nanoscale”, *Advanced Materials*, 16(15), 1271–1293 (2004).

9. G. Joshi, H. Lee, Y. Lan, X. Wang, G. Zhu, D. Wang, R. W. Gould, D. C. Cuff, M. Y. Tang, M. S. Dresselhaus, G. Chen, and Z. Ren. “Enhanced thermoelectric figure-of-merit in nanostructured p-type silicon germanium bulk alloys”, *Nano Letters*, 8(12), 4670–4674 (2008).

10. E. T. Thostenson, C. Li, and T.-W. Chou. “Nanocomposites in context”, *Composites Science and Technology*, 65(3-4), 491–516 (2005).

11. Z.-M. Dang, B. Xia, S.-H Yao, M.-J. Jiang, H.-T. Song, L.-Q. Zhang, and D. Xie. “High-dielectric-permittivity high-elasticity three-component nanocomposites with low percolation threshold and low dielectric loss”, *Applied Physics Letters*, 94(4), 042902 (2009).

12. S. Rezanejad and M. Kokabi. “Shape memory and mechanical properties of cross-linked polyethylene/clay nanocomposites”, *European Polymer Journal*, 43(7), 2856–2865 (2007).

13. R. Yang and G. Chen. “Thermal conductivity modeling of periodic two-dimensional nanocomposites”, *Physical Review B*, 69, 195316 (2004).

14. F. Hussain, M. Hojjati, M. Okamoto, and R. E. Gorga. "Review article: Polymer-matrix nanocomposites, processing, manufacturing, and application: An overview", *Journal of Composite Materials*, 40(17), 1511–1575 (2006).

15. R. A. Hule and D. J. Pochan. "Polymers nanocomposites for biomedical applications", *MRS Bulletin*, 32, 354–358 (2007).

16. M. Song, C. Pan, C. Chen, J. Li, X. Wang, and Z. Gu. "The application of new nanocomposites: Enhancement effect of polylactide nanofibers/nano-TiO2 blends on biorecognition of anticancer drug daunorubicin", *Applied Surface Science*, 255(2), 610–612 (2008).

17. C. Li, E. T. Thostenson, and T.-W. Chou. "Sensors and actuators based on carbon nanotubes and their composites: A review", *Composites Science and Technology*, 68(6), 1227–1249 (2008).

18. G. Hunter, R. V. Wal, L. Evans, J. Xu, G. Berger, M. Kullis, A. Biaggi-Labiosa, "Nanostructured material sensor processing using microfabrication techniques", *Sensor Review*, 32(2), 106 – 117 (2012).

19. W. Xie, J. He, H. J. Kang, X. Tang, S. Zhu, M. Laver, S. Wang, J. R. D. Copley, C. M. Brown, Q. Zhang, and T. M. Tritt. "Identifying the specific nanostructures responsible for the high thermoelectric performance of (Bi,Sb)2Te3 nanocomposites", *Nano Letters*, 10(9), 3283–3289 (2010).

20. X. Yan, G. Joshi, W. Liu, Y. Lan, H. Wang, S. Lee, J. W. Simonson, S. J. Poon, T. M. Tritt, Gang Chen, and Z. F. Ren, "Enhanced Thermoelectric Figure of Merit of p-Type Half-Heuslers", *Nano Letters*, 11(2), 556–560 (2011).

21. C. M. Snowden and E. Snowden. Introduction to Semiconductor Device Modeling. World Scientific (1987).

22. H. Li, Y. Xu, Y. Xu and G. Li, "Strain effect analysis on the electrical conductivity of Si/$_{Si1-x}$Ge$_x$ nanocomposite thin films", under review, 2012.

23. H. K. Gummel and H. C. Poon, "An integral charge-control model of bipolar transistors," *Bell Systems Technical Journal*, 49, 827–852 (1970).

24. T. M. Abdolkader, W. F. Farouk, O. A. Omar and M. F. M. Hassan. "FETMOSS: a software tool for 2D simulation of double-gate MOSFET", *International Journal of Numerical Modeling: Electronic Networks, Devices and Fields*, 19, 301-314 (2006).

25. F. J. C. Ruiz, A. Godoy, F. Gamiz, C. Sampedro and L. Donetti. "A comprehensive study of the corner effects in pi-gate MOSFETs including quantum effects", *IEEE Transaction of Electron Devices*, 54(12), 3369-3377 (2007).

26. A. Trellakis, A.T. Galick, A. Pacelli and U. Ravaioli. "Iteration scheme for the solution of the two-dimensional Schrodinger-Poisson equations in quantum structures", *Journal of Applied Physics*, 81, 7880 (1997).

27. C. S. Lent and D. J. Kirkner. “The quantum transmitting boundary method”, *Journal of Applied Physics*, 67(10) , 6353-6359 (1990).

28. S. E. Laux, A Kumar and V. Fishetti. “Analysis of quantum ballistic electron transport in ultrasmall silicon devices including space-charge and geometric effects”, *Journal of Applied Physics*, 95(10), 5545-5582 (2004).

29. Z. Ren, R. Venugopal, S. Goasguen, S. Datta and M. Lundstrom. “nanoMOS 2.5: A two-dimensional simulator for quantum transport in double-gate MOSFETs”, *IEEE Transactions on Electron Devices*, 50(9), 2003.

30. S. Datta, Electronic Transport in Mesoscopic Systems, Cambridge University Press, Cambridge, UK, 1997.

31. R. Biswas, C.Z. Wang, K.M. Ho, C.M. Soukoulis. Transferable Tight Binding Models for Silicon. *Physical Review B* 49, 7242-7250 (1994).

32. J. C. Slater and G. F. Koster, ``Simplified LCAO Method for the Periodic Potential Problem," *Physical Review*, 94, 1498-1524 (1954).

33. N. Argaman, G. Makov. “Density functional theory-An introduction”, *American Journal of Physics*, 68(1), 69-79 (2000).

34. P. Ordejon, J. Soler, E. Artacho. “Self-consistent order-N density-functional calculations for very large systems”, *Physical Review B*, 53(16), 10441-10444 (1996).

35. R. Craig and M. Bampton. “Coupling of substructures for dynamic analysis”, AIAA Journal 6, 1313 (1968).

36. M. A. Tournour, N. Atalla, O. Chiello, F. Sgard. “Validation, performance, convergence and application of free interface component mode synthesis”, *Computers and Structures*, 79, 1861–1876 (2001).

37. G. Li, "A Multilevel Component Mode Synthesis Approach for the Calculation of the Phonon Density of States of Nanocomposite Structures," *Computational Mechanics*, 42(4), 593-606 (2008).

38. M. T. Heath, Scientific Computing: An Introductory Survey, 2nd Ed. McGraw Hill, 2002.

39. H. Li and G. Li, “Component mode synthesis approaches for quantum mechanical electrostatic analysis of nanoscale devices”, *Journal of Computational Electronics*, 10(3), 300-313 (2011).

40. X. Sun, Q. Lu, V. Moroz, H. Takeuchi, G. Gebara, J. Wetzel, S. Ikeda, C. Shin and T. K. Liu. “Tri-gate bulk MOSFET design for CMOS scaling to the end of the roadmap”, *IEEE Electron Device Letters*, 29(5), 491-493 (2008).